

POLITECNICO DI TORINO

M.Sc. in Electronic Engineering

Master's thesis

Optimization of low-profile directive antennas



Advisor:

Prof. Giuseppe Vecchi

Co-advisors:

Dott. Giorgio Giordanengo

Dott. Marco Righero

Candidate:

Marcello Zucchi

ACADEMIC YEAR 2017-2018

Acknowledgements

“Computational resources provided by HPC@POLITO, which is a project of Academic Computing within the Department of Control and Computer Engineering at the Politecnico di Torino (<http://hpc.polito.it>)”

Contents

1	Introduction	1
1.1	Directive antennas	1
1.2	Optimization strategies	2
1.3	Objective	2
2	Electromagnetic formulation	4
2.1	EM radiation in homogeneous space	4
2.1.1	Vector wave equation	4
2.1.2	Boundary conditions	5
2.1.3	Green's function	6
2.1.4	Field-source relations in homogeneous space	7
2.2	Radiation and scattering formulation	8
2.2.1	Surface Equivalence Theorem	8
2.2.2	Surface Integral Equation	9
2.3	Antenna parameters	14
2.3.1	Input matching	14
2.3.2	Far-field radiation	15
2.3.3	Effective area	16
2.3.4	Beam efficiency	17
3	Computational electromagnetics	18
3.1	Method of Moments for electromagnetic simulation	18
3.1.1	Method of Moments formulation	19
3.1.2	Basis functions	20
3.1.3	Discretization by Galerkin's method and RWG basis functions	22
3.1.4	Source modeling	26
3.2	Analysis of multiport structures	27
3.3	Far Field calculation	28
4	Optimization techniques in antenna design	30
4.1	Genetic algorithms	30
4.1.1	Evolutionary operators	31

4.1.2	Optimization flow	33
4.2	Local optimization	37
4.3	GA and MoM for antenna design	37
5	Optimization of low-profile directive antennas	40
5.1	Preprocessing	41
5.2	Matrix manipulation	42
5.2.1	Metal structures	43
5.2.2	Composite metal/dielectric structures	43
5.3	Fitness function	47
5.4	Computational cost reduction techniques	49
5.4.1	Geometric symmetry	49
5.4.2	Code parallelization	52
6	Results	53
6.1	Optimization of multiband antenna	53
6.2	Pin fed planar antenna	59
6.2.1	Infinite ground plane	59
6.2.2	Finite ground plane	59
6.2.3	Coaxial feed	61
6.3	Slot coupled microstrip planar antenna	65
6.4	Modeling evaluation	69
6.4.1	Effect of mesh singularities	69
6.4.2	Mesh size	70
6.5	Prototyping	72
6.5.1	Layout	72
7	Conclusions	74
	Appendix A GiD <i>Problem type</i>	75
	Appendix B Matlab code	77
B.1	MoM solver	77
B.2	Fitness function	83
	Bibliography	86

Chapter 1

Introduction

1.1 Directive antennas

Directive antennas are a class of radiators able to concentrate the radiated energy in a narrow beam around a given direction. They are specifically used in those applications where a precise targeting is needed, like in point-to-point links and radar.

Due to physical limitations, they are inherently narrowband, with directivity proportional to their size [7]. As such, they are usually realized by means of electrically large structures (e.g. parabolic reflector, helix antenna, etc.) with obvious drawbacks due to space occupation.

Large values of directivity can be also achieved by arranging multiple small elements in arrays, with specific geometric and feeding constraints. This technique has the advantage of being low-profile, meaning that they take less space than usual (Fig. 1.1). However, the complexity and losses introduced by the feeding network limit their performances. In the present work, the starting point is represented by

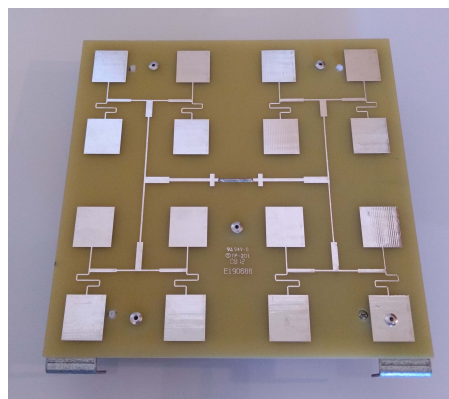


Figure 1.1: A 4-by-4 patch array working at 2.4 GHz

simple structures, finely optimized to obtain non-intuitive geometries which meet the required performances.

1.2 Optimization strategies

Optimization is classically carried out by parameterizing the antenna with respect to a small set of essential features, then optimizing this reduced model. This approach has inherent limits, given that antenna structures can rarely be described using a limited set of parameters.

Historically, most of the effort has been devoted to deterministic optimization methods. However, electromagnetic problems usually present non-linear, non-differentiable and unconstrained objective functions, which often lead to premature convergence to local minima. For this reason, in the last decades the use of global optimization strategies is favored, thanks to their stochastic nature and ability to deal effectively with large solution spaces and non-differentiable functions. Among them, Genetic Algorithms (GA), which are based on principles derived from natural evolution, have been applied successfully to a number of electromagnetic problems [18].

For the aforementioned reasons, in [11] a novel technique was introduced to combine the Method of Moments (MoM) with Genetic Algorithms to perform full-wave optimization. It allows to fill the matrix resulting from the discretization only once during the setup phase. Modification to the structure are accounted for by eliminating rows and columns corresponding to removed parts.

Despite all that, optimization tools still suffer from the lack of physical insight into antenna behaviour. Therefore, algorithms need to be fine-tuned with the knowledge available to the designer, through the definition of objective functions able to express feasible goals and trade-offs commonly found in antenna design.

1.3 Objective

The present work is based on [14], where the GA/MoM algorithm was applied to the optimization of compact frequency reconfigurable antennas. Reconfigurability was achieved by means of switches integrated into the antenna. Each structure was analyzed as a multiport equivalent circuit, with an exhaustive search of switch configurations, with focus on the achieved input matching over a wide frequency range.

Regarding directive antennas, Genetic algorithms have been applied extensively to the optimization of arrays [4, 12] due to a convenient mathematical formulation. To apply a full-wave optimization to arbitrary structures, a need arises to decouple the discretization mesh from the optimization process, since large geometries require a finer resolution.

This work presents the development of optimization tools capable of handling complex structures, like those needed for directive antennas, by allowing the designer to define custom optimizable geometries of arbitrary size and shape, all within the preprocess phase.

The thesis will be organized as follows: **Chapter 2** recalls the electromagnetic theory underlying this work. **Chapter 3** introduces the Method of Moments applied to electromagnetic problems. **Chapter 4** covers the optimization algorithms employed. The results of theoretical and practical activities are presented in **Chapter 5** and **6**. Finally, in **Chapter 7** conclusions are drawn and future developments are suggested.

Chapter 2

Electromagnetic formulation

This chapter is devoted to the presentation of the general electromagnetic theory that allows to solve scattering and radiation problems. In section 2.1 the wave equation is derived from Maxwell's equations, and an expression for the radiated field is obtained in terms of electric and magnetic source currents. In section 2.2 an equivalence theorem will be introduced which will allow to derive an integral equation for the solution of source currents, known as *Surface Integral Equation* formulation (SIE). Finally, in section 2.3.1, a series of parameters for the analysis of antennas will be presented.

2.1 EM radiation in homogeneous space

2.1.1 Vector wave equation

Maxwell's equations in frequency domain (time variation $e^{j\omega t}$) for a homogeneous isotropic media of constitutive parameters ε and μ can be written as [10]:

$$\nabla \times \mathbf{E} = -j\omega\mu\mathbf{H} - \mathbf{M} \quad (2.1)$$

$$\nabla \times \mathbf{H} = j\omega\varepsilon\mathbf{E} + \mathbf{J} \quad (2.2)$$

$$\nabla \cdot \mathbf{E} = \frac{\rho_e}{\varepsilon} \quad (2.3)$$

$$\nabla \cdot \mathbf{H} = \frac{\rho_m}{\mu} \quad (2.4)$$

where $\mu = \mu_r\mu_0$ and $\varepsilon = \varepsilon_r\varepsilon_0$. The magnetic current \mathbf{M} and charge density ρ_m have no physical meaning, but are introduced because of their usefulness in the derivation of equivalence theorems.

Electric and magnetic currents are related to the corresponding charge densities

by the continuity equations

$$\nabla \cdot \mathbf{J} = -j\omega\rho_e \quad (2.5)$$

$$\nabla \cdot \mathbf{M} = -j\omega\rho_m \quad (2.6)$$

Eqs. (2.1)–(2.4) combined with Eqs. (2.5)–(2.6), allow the determination of fields \mathbf{E} , \mathbf{H} in terms of the source currents \mathbf{J} , \mathbf{M} only. The resulting equations are known as *vector wave equations*:

$$\nabla^2 \mathbf{E} + k^2 \mathbf{E} = j\omega\mu\mathbf{J} - \frac{1}{j\omega\varepsilon} \nabla(\nabla \cdot \mathbf{J}) + \nabla \times \mathbf{M} \quad (2.7)$$

$$\nabla^2 \mathbf{H} + k^2 \mathbf{H} = j\omega\varepsilon\mathbf{M} - \frac{1}{j\omega\mu} \nabla(\nabla \cdot \mathbf{M}) - \nabla \times \mathbf{J} \quad (2.8)$$

where $k = \omega\sqrt{\mu\varepsilon}$ is the wavenumber in the medium.

The same vector wave equation can be written in terms of magnetic vector potential \mathbf{A} and electric vector potential \mathbf{F} as:

$$\nabla^2 \mathbf{A} + k^2 \mathbf{A} = -\mu\mathbf{J} \quad (2.9)$$

$$\nabla^2 \mathbf{F} + k^2 \mathbf{F} = -\varepsilon\mathbf{M} \quad (2.10)$$

Once eqs. (2.9) and (2.10) are solved, the electric and magnetic fields are given by:

$$\mathbf{E} = -j\omega\mathbf{A} + \frac{1}{j\omega\mu\varepsilon} \nabla(\nabla \cdot \mathbf{A}) - \frac{1}{\varepsilon} \nabla \times \mathbf{F} \quad (2.11)$$

$$\mathbf{H} = \frac{1}{\mu} \nabla \times \mathbf{A} - j\omega\mathbf{F} + \frac{1}{j\omega\mu\varepsilon} \nabla(\nabla \cdot \mathbf{F}) \quad (2.12)$$

2.1.2 Boundary conditions

For the solution of Eqs. (2.7) and (2.8), we also need boundary conditions. At the interface between two materials with constitutive parameters ε_1, μ_1 and ε_2, μ_2 we have:

$$\hat{\mathbf{n}} \times (\mathbf{H}_2 - \mathbf{H}_1) = \mathbf{J}_s \quad (2.13)$$

$$\hat{\mathbf{n}} \times (\mathbf{E}_2 - \mathbf{E}_1) = -\mathbf{M}_s \quad (2.14)$$

$$\hat{\mathbf{n}} \cdot (\varepsilon_2 \mathbf{E}_2 - \varepsilon_1 \mathbf{E}_1) = \rho_{e,s} \quad (2.15)$$

$$\hat{\mathbf{n}} \cdot (\mu_2 \mathbf{H}_2 - \mu_1 \mathbf{H}_1) = \rho_{m,s} \quad (2.16)$$

where $\hat{\mathbf{n}}$ is the unit vector normal to the interface, \mathbf{J}_s and \mathbf{M}_s are surface current densities and $\rho_{e,s}$, $\rho_{m,s}$ are surface charge densities.

Since the surface between two dielectrics cannot support surface currents or

charges, Eqs. (2.13)–(2.16) reduce to:

$$\hat{\mathbf{n}} \times (\mathbf{H}_2 - \mathbf{H}_1) = \mathbf{0} \quad \longrightarrow \quad \mathbf{H}_2^t = \mathbf{H}_1^t \quad (2.17)$$

$$\hat{\mathbf{n}} \times (\mathbf{E}_2 - \mathbf{E}_1) = \mathbf{0} \quad \longrightarrow \quad \mathbf{E}_2^t = \mathbf{E}_1^t \quad (2.18)$$

$$\hat{\mathbf{n}} \cdot (\varepsilon_2 \mathbf{E}_2 - \varepsilon_1 \mathbf{E}_1) = 0 \quad \longrightarrow \quad \varepsilon_2 \mathbf{E}_2^n = \varepsilon_1 \mathbf{E}_1^n \quad (2.19)$$

$$\hat{\mathbf{n}} \cdot (\mu_2 \mathbf{H}_2 - \mu_1 \mathbf{H}_1) = 0 \quad \longrightarrow \quad \mu_2 \mathbf{H}_2^n = \mu_1 \mathbf{H}_1^n \quad (2.20)$$

Eqs. (2.17)–(2.18) express the continuity of tangential component, while (2.19)–(2.20) state that the normal component is discontinuous due to different constitutive parameters on each side.

For a perfect electric conductor (PEC) instead, surface electric charge and current densities are induced by an external electromagnetic field and $\mathbf{E} = \mathbf{H} = \mathbf{0}$ everywhere inside. Boundary conditions become:

$$\hat{\mathbf{n}} \times (\mathbf{H} - \mathbf{0}) = \mathbf{J}_s \quad \longrightarrow \quad \hat{\mathbf{n}} \times \mathbf{H} = \mathbf{J}_s \quad (2.21)$$

$$\hat{\mathbf{n}} \times (\mathbf{E} - \mathbf{0}) = \mathbf{0} \quad \longrightarrow \quad \mathbf{E}^t = \mathbf{0} \quad (2.22)$$

$$\hat{\mathbf{n}} \cdot (\varepsilon \mathbf{E} - \mathbf{0}) = \rho_{e,s} \quad \longrightarrow \quad \mathbf{E}^n = \frac{\rho_{e,s}}{\varepsilon} \hat{\mathbf{n}} \quad (2.23)$$

$$\hat{\mathbf{n}} \cdot (\mu \mathbf{H} - \mathbf{0}) = 0 \quad \longrightarrow \quad \mathbf{H}^n = \mathbf{0} \quad (2.24)$$

Eq. (2.21) relates the tangent component of magnetic field to the surface current density, Eq. (2.22) forces the tangential electric field to vanish on a PEC surface. Eq. (2.23) relates the normal component of electric field to the surface electric charge and finally Eq. (2.24) imposes the normal magnetic field to vanish on the surface.

For an unbounded domain, the only requirement is for the field to vanish at infinity according to the *Sommerfeld radiation condition* [20]

$$\lim_{|\mathbf{r}| \rightarrow \infty} |\mathbf{r}| (\nabla \times \mathbf{E} + jk \hat{\mathbf{r}} \times \mathbf{E}) = \mathbf{0} \quad (2.25)$$

$$\lim_{|\mathbf{r}| \rightarrow \infty} |\mathbf{r}| (\nabla \times \mathbf{H} + jk \hat{\mathbf{r}} \times \mathbf{H}) = \mathbf{0} \quad (2.26)$$

2.1.3 Green's function

One way to solve Eqs. (2.9) and (2.10) is to first find the solution due to a point source in an unbounded homogeneous domain:

$$\nabla^2 G(\mathbf{r}, \mathbf{r}') + k^2 G(\mathbf{r}, \mathbf{r}') = -\delta(\mathbf{r} - \mathbf{r}') \quad (2.27)$$

where $G(\mathbf{r}, \mathbf{r}')$ is the *Green's function*, or *fundamental solution*, of the problem. $\delta(\mathbf{r} - \mathbf{r}')$ is called the *Dirac delta function* and is defined as

$$\delta(\mathbf{r} - \mathbf{r}') = 0 \quad \text{if } \mathbf{r} \neq \mathbf{r}'$$

$$\int_{\mathcal{D}} \delta(\mathbf{r} - \mathbf{r}') d\mathcal{D}' = \begin{cases} 1 & \text{if } \mathbf{r} \in \mathcal{D} \\ 0 & \text{if } \mathbf{r} \notin \mathcal{D} \end{cases}$$

due to these properties, it follows that for a function $f(\mathbf{r})$ continuous at point \mathbf{r}

$$\int_{\mathcal{D}} f(\mathbf{r}') \delta(\mathbf{r} - \mathbf{r}') d\mathcal{D}' = \begin{cases} f(\mathbf{r}) & \text{if } \mathbf{r} \in \mathcal{D} \\ 0 & \text{if } \mathbf{r} \notin \mathcal{D} \end{cases}$$

The solution of Eq. (2.27) in a three-dimensional unbounded domain, subject to radiation boundary conditions, is given by:

$$G(\mathbf{r}, \mathbf{r}') = \frac{e^{-jk|\mathbf{r}-\mathbf{r}'|}}{4\pi|\mathbf{r}-\mathbf{r}'|} \quad (2.28)$$

This solution represents a scalar spherical wave propagating away from point \mathbf{r}' .

2.1.4 Field-source relations in homogeneous space

Once the Green's function is found for a specific domain, the vector potentials can be written in terms of source currents:

$$\mathbf{A}(\mathbf{r}) = \mu \int_{\mathcal{D}} \mathbf{J}(\mathbf{r}') G(\mathbf{r}, \mathbf{r}') d\mathcal{D}' \quad (2.29)$$

$$\mathbf{F}(\mathbf{r}) = \varepsilon \int_{\mathcal{D}} \mathbf{M}(\mathbf{r}') G(\mathbf{r}, \mathbf{r}') d\mathcal{D}' \quad (2.30)$$

These can be plugged into Eqs. (2.11) and (2.12) to find the complete source-field relation in an homogeneous space:

$$\mathbf{E}(\mathbf{r}) = \int_{\mathcal{D}} \left\{ -j\omega\mu \mathbf{J}(\mathbf{r}') + \frac{1}{j\omega\varepsilon} \nabla' [\nabla' \cdot \mathbf{J}(\mathbf{r}')] - \nabla' \times \mathbf{M}(\mathbf{r}') \right\} G(\mathbf{r}, \mathbf{r}') d\mathcal{D}' \quad (2.31)$$

$$\mathbf{H}(\mathbf{r}) = \int_{\mathcal{D}} \left\{ -j\omega\varepsilon \mathbf{M}(\mathbf{r}') + \frac{1}{j\omega\mu} \nabla' [\nabla' \cdot \mathbf{M}(\mathbf{r}')] + \nabla' \times \mathbf{J}(\mathbf{r}') \right\} G(\mathbf{r}, \mathbf{r}') d\mathcal{D}' \quad (2.32)$$

We can define two linear operator \mathcal{L} and \mathcal{K} as:

$$\mathcal{L}[\mathbf{X}] = jk \int_{\mathcal{D}} G(\mathbf{r}, \mathbf{r}') \mathbf{X}(\mathbf{r}') d\mathcal{D}' - \frac{1}{jk} \nabla \int_{\mathcal{D}} G(\mathbf{r}, \mathbf{r}') \nabla' \cdot \mathbf{X}(\mathbf{r}') d\mathcal{D}' \quad (2.33)$$

$$\mathcal{K}[\mathbf{X}] = \int_{\mathcal{D}} \mathbf{X}(\mathbf{r}') \times \nabla G(\mathbf{r}, \mathbf{r}') d\mathcal{D}' \quad (2.34)$$

with this definition, Eqs. (2.31) and (2.32) can be rewritten as:

$$\mathbf{E}(\mathbf{r}) = -\eta \mathcal{L}[\mathbf{J}](\mathbf{r}) + \mathcal{K}[\mathbf{M}](\mathbf{r}) \quad (2.35)$$

$$\mathbf{H}(\mathbf{r}) = -\mathcal{K}[\mathbf{J}](\mathbf{r}) - \frac{1}{\eta} \mathcal{L}[\mathbf{M}](\mathbf{r}) \quad (2.36)$$

where $\eta = \sqrt{\mu/\varepsilon}$ is the wave impedance in the medium.

2.2 Radiation and scattering formulation

2.2.1 Surface Equivalence Theorem

The formulation of the electromagnetic problem in terms of a surface integral relies on the *uniqueness theorem* [10, 3] which states that in a lossy domain where sources \mathbf{J} and \mathbf{M} radiate, the field solution is unique if the tangential component of \mathbf{E} or \mathbf{H} is specified on the boundary of the domain.

This allows to develop a *Surface Equivalence Theorem*: consider a volume V_1 with parameters ε_1, μ_1 and a volume V_2 with ε_2, μ_2 completely inside it. In V_1 , sources radiate a field $\mathbf{E}^{\text{inc}}, \mathbf{H}^{\text{inc}}$ in homogeneous space (Fig. 2.1a).

Thanks to the uniqueness theorem, the solution $\mathbf{E}_1^{\text{tot}}, \mathbf{H}_1^{\text{tot}}$ is the same as if we choose the field inside V_2 arbitrarily, and put equivalent current sources on the surface S to satisfy the boundary conditions of the original problem.

Since the field in V_2 can be chosen freely (as long as it is a solution of Maxwell's equations), one particular choice is to set it to 0 everywhere (*Love's theorem* or *Extinction theorem* [3]). To compensate the field discontinuity on surface S , according to boundary conditions (2.17)–(2.18), we need:

$$\mathbf{J}_1 = \hat{\mathbf{n}}_1 \times (\mathbf{H}_1^{\text{tot}} - \mathbf{0}) = \hat{\mathbf{n}}_1 \times \mathbf{H}_1^{\text{tot}} \quad (2.37)$$

$$\mathbf{M}_1 = -\hat{\mathbf{n}}_1 \times (\mathbf{E}_1^{\text{tot}} - \mathbf{0}) = -\hat{\mathbf{n}}_1 \times \mathbf{E}_1^{\text{tot}} \quad (2.38)$$

where the normal unit vector $\hat{\mathbf{n}}_1$ points inside V_1 .

This choice allows to modify the medium inside V_2 without affecting the solution. If we assign the constitutive parameters ε_1, μ_1 the equivalent problem in V_1 reduces to that of a set of equivalent currents \mathbf{J}_1 and \mathbf{M}_1 radiating in a homogeneous unbounded medium superimposed to the incident field already present in the

absence of the scatterer (Fig. 2.1b):

$$\mathbf{E}_1^{\text{tot}} = \mathbf{E}^{\text{inc}} + \mathbf{E}_1^{\text{s}}(\mathbf{J}_1, \mathbf{M}_1) \quad (2.39)$$

$$\mathbf{H}_1^{\text{tot}} = \mathbf{H}^{\text{inc}} + \mathbf{H}_1^{\text{s}}(\mathbf{J}_1, \mathbf{M}_1) \quad (2.40)$$

where \mathbf{E}^{s} and \mathbf{H}^{s} , the *scattered fields*, can be evaluated with Eqs. (2.35) and (2.36).

The same reasoning can be applied to V_2 (Fig. (2.1c)). In this case, a set of equivalent current \mathbf{J}_2 and \mathbf{M}_2 are defined on surface S such that the field outside is equal to 0 everywhere, and equal to the original field inside the surface.

$$\mathbf{J}_2 = \hat{\mathbf{n}}_2 \times (\mathbf{H}_2^{\text{tot}} - \mathbf{0}) = \hat{\mathbf{n}}_2 \times \mathbf{H}_1^{\text{tot}} \quad (2.41)$$

$$\mathbf{M}_2 = -\hat{\mathbf{n}}_2 \times (\mathbf{E}_2^{\text{tot}} - \mathbf{0}) = -\hat{\mathbf{n}}_2 \times \mathbf{E}_1^{\text{tot}} \quad (2.42)$$

this time $\hat{\mathbf{n}}_2$ points toward V_2 . Internal fields can be written as:

$$\mathbf{E}_2^{\text{tot}} = \mathbf{E}_2^{\text{s}}(\mathbf{J}_2, \mathbf{M}_2) \quad (2.43)$$

$$\mathbf{H}_2^{\text{tot}} = \mathbf{H}_2^{\text{s}}(\mathbf{J}_2, \mathbf{M}_2) \quad (2.44)$$

These equivalent settings can be used to develop integral formulations that are suitable to approximation and solution with the help of numerical methods.

2.2.2 Surface Integral Equation

The equivalent problems presented in Sec. 2.2.1 allows to formulate the radiation and scattering problems as integral equations [21]. Focusing on the equivalent problem in V_1 , Eqs. (2.39) and (2.40) on surface S imply

$$\left[\mathbf{E}^{\text{inc}} + \mathbf{E}_1^{\text{s}}(\mathbf{J}_1, \mathbf{M}_1) \right]_{\text{tan}} = \left[\mathbf{E}_1^{\text{tot}} \right]_{\text{tan}} \quad (2.45)$$

$$\left[\mathbf{H}^{\text{inc}} + \mathbf{H}_1^{\text{s}}(\mathbf{J}_1, \mathbf{M}_1) \right]_{\text{tan}} = \left[\mathbf{H}_1^{\text{tot}} \right]_{\text{tan}} \quad (2.46)$$

The fields components tangent to the surface can be expressed in terms of equivalent currents (2.37) and (2.38) as:

$$\left[\mathbf{E}_1^{\text{tot}} \right]_{\text{tan}} = \hat{\mathbf{n}}_1 \times \mathbf{M}_1 \quad (2.47)$$

$$\left[\mathbf{H}_1^{\text{tot}} \right]_{\text{tan}} = -\hat{\mathbf{n}}_1 \times \mathbf{J}_1 \quad (2.48)$$

Thus we can write Eqs. (2.45)–(2.46) in terms of known incident field and unknown equivalent currents as:

$$\left[\mathbf{E}_1^s(\mathbf{J}_1, \mathbf{M}_1) \right]_{\text{tan}} - \hat{\mathbf{n}}_1 \times \mathbf{M}_1 = - \left[\mathbf{E}^{\text{inc}} \right]_{\text{tan}} \quad (2.49)$$

$$\left[\mathbf{H}_1^s(\mathbf{J}_1, \mathbf{M}_1) \right]_{\text{tan}} + \hat{\mathbf{n}}_1 \times \mathbf{J}_1 = - \left[\mathbf{H}^{\text{inc}} \right]_{\text{tan}} \quad (2.50)$$

Using the radiation operators (2.35) and (2.36), we can further develop these expressions:

$$\left[-\eta_1 \mathcal{L}_1[\mathbf{J}_1] + \mathcal{K}_1[\mathbf{M}_1] \right]_{\text{tan}} - \hat{\mathbf{n}}_1 \times \mathbf{M}_1 = - \left[\mathbf{E}^{\text{inc}} \right]_{\text{tan}} \quad (2.51)$$

$$\left[-\mathcal{K}_1[\mathbf{J}_1] - \frac{1}{\eta_1} \mathcal{L}_1[\mathbf{M}_1] \right]_{\text{tan}} + \hat{\mathbf{n}}_1 \times \mathbf{J}_1 = - \left[\mathbf{H}^{\text{inc}} \right]_{\text{tan}} \quad (2.52)$$

The operator \mathcal{K} is singular when we evaluate it in a point inside its domain [10]. In this particular case, we can express it as:

$$\mathcal{K}[\mathbf{X}](\mathbf{r}) = \mathcal{K}^{\text{PV}}[\mathbf{X}](\mathbf{r}) + \frac{1}{2} \hat{\mathbf{n}} \times \mathbf{X}(\mathbf{r}) \quad \mathbf{r} \in S \quad (2.53)$$

taking into account this singularity, Eqs. (2.51)–(2.52) become

$$\left[\eta_1 \mathcal{L}_1[\mathbf{J}_1] - \mathcal{K}_1^{\text{PV}}[\mathbf{M}_1] \right]_{\text{tan}} + \frac{1}{2} \hat{\mathbf{n}}_1 \times \mathbf{M}_1 = \left[\mathbf{E}^{\text{inc}} \right]_{\text{tan}} \quad (2.54)$$

$$\left[\mathcal{K}_1^{\text{PV}}[\mathbf{J}_1] + \frac{1}{\eta_1} \mathcal{L}_1[\mathbf{M}_1] \right]_{\text{tan}} - \frac{1}{2} \hat{\mathbf{n}}_1 \times \mathbf{J}_1 = \left[\mathbf{H}^{\text{inc}} \right]_{\text{tan}} \quad (2.55)$$

Eq. (2.54) is known as *Electric Field Integral Equation* (EFIE), while Eq. (2.55) is called *Magnetic Field Integral Equation* (MFIE), since they involve the tangential electric and magnetic fields respectively.

An alternative formulation can be obtained by taking the cross product of (2.54)–(2.55) with $\hat{\mathbf{n}}$:

$$\hat{\mathbf{n}}_1 \times \left(\eta_1 \mathcal{L}_1[\mathbf{J}_1] - \mathcal{K}_1^{\text{PV}}[\mathbf{M}_1] \right) - \frac{1}{2} \mathbf{M}_1 = \hat{\mathbf{n}}_1 \times \mathbf{E}^{\text{inc}} \quad (2.56)$$

$$\hat{\mathbf{n}}_1 \times \left(\mathcal{K}_1^{\text{PV}}[\mathbf{J}_1] + \frac{1}{\eta_1} \mathcal{L}_1[\mathbf{M}_1] \right) + \frac{1}{2} \mathbf{J}_1 = \hat{\mathbf{n}}_1 \times \mathbf{H}^{\text{inc}} \quad (2.57)$$

These equations are called *Normal–Electric Field Integral Equation* (N-EFIE) and *Normal–Magnetic Field Integral Equation* (N-MFIE) respectively. To distinguish between the two, Eqs. (2.54) and (2.55) are also referred to as tangential equations, T-EFIE and T-MFIE.

We can also write integral equations for the volume V_2 . In this case, the incident field is null inside the volume. The integral equations become:

$$\left[\eta_2 \mathcal{L}_2[\mathbf{J}_2] - \mathcal{K}_2^{\text{PV}}[\mathbf{M}_2] \right]_{\text{tan}} + \frac{1}{2} \hat{\mathbf{n}}_2 \times \mathbf{M}_2 = \mathbf{0} \quad (\text{T-EFIE})$$

$$\left[\mathcal{K}_2^{\text{PV}}[\mathbf{J}_2] + \frac{1}{\eta_2} \mathcal{L}_2[\mathbf{M}_2] \right]_{\text{tan}} - \frac{1}{2} \hat{\mathbf{n}}_2 \times \mathbf{J}_2 = \mathbf{0} \quad (\text{T-MFIE})$$

$$\hat{\mathbf{n}}_2 \times \left(\eta_2 \mathcal{L}_2[\mathbf{J}_2] - \mathcal{K}_2^{\text{PV}}[\mathbf{M}_2] \right) - \frac{1}{2} \mathbf{M}_2 = \mathbf{0} \quad (\text{N-EFIE})$$

$$\hat{\mathbf{n}}_2 \times \left(\mathcal{K}_2^{\text{PV}}[\mathbf{J}_2] + \frac{1}{\eta_2} \mathcal{L}_2[\mathbf{M}_2] \right) + \frac{1}{2} \mathbf{J}_2 = \mathbf{0} \quad (\text{N-MFIE})$$

These equations cannot be solved analytically, but are suited to numerical approximations, as will be seen in chapter 3.

At the resonance frequencies of the structure, the solution of these equations is not unique and the condition number of the discretized system will be high, yielding unreliable results. Since the resonances for the EFIE and MFIE are not the same, a linear combination of these two equations will guarantee a robust solution [8].

Linear operators $\frac{1}{\eta} [\mathbf{E}^s(\mathbf{J}, \mathbf{M})]_{\text{tan}}$ and $\hat{\mathbf{n}} \times \mathbf{H}^s(\mathbf{J}, \mathbf{M})$ map the surface currents (\mathbf{J}, \mathbf{M}) to the space of tangential electric currents \mathbf{J} , while operators $\eta [\mathbf{H}^s(\mathbf{J}, \mathbf{M})]_{\text{tan}}$ and $\hat{\mathbf{n}} \times \mathbf{E}^s(\mathbf{J}, \mathbf{M})$ map the surface currents (\mathbf{J}, \mathbf{M}) to the space of tangential electric currents \mathbf{M} . For this reason, a well conditioned system is obtained by combining the different formulations as follows [19]:

$$a \frac{1}{\eta} \text{T-EFIE} + b \text{N-MFIE} \quad (2.58)$$

$$-c \text{N-EFIE} + d \eta \text{T-MFIE} \quad (2.59)$$

These combinations are known as *Combined Field Integral Equation* (CFIE).

Scattering by a dielectric

If medium 1 and 2 are both dielectric, boundary conditions (2.17)–(2.18) force the tangential components of the electric and magnetic fields to be equal on S . With regard to Eqs. (2.47) and (2.48) and corresponding ones in medium 2, we derive

$$\begin{aligned} \left[\mathbf{E}_1^{\text{tot}} \right]_{\text{tan}} = \left[\mathbf{E}_2^{\text{tot}} \right]_{\text{tan}} &\longrightarrow \hat{\mathbf{n}}_1 \times \mathbf{M}_1 = \hat{\mathbf{n}}_2 \times \mathbf{M}_2 \\ \left[\mathbf{H}_1^{\text{tot}} \right]_{\text{tan}} = \left[\mathbf{H}_2^{\text{tot}} \right]_{\text{tan}} &\longrightarrow -\hat{\mathbf{n}}_1 \times \mathbf{J}_1 = -\hat{\mathbf{n}}_2 \times \mathbf{J}_2 \end{aligned}$$

since $\hat{\mathbf{n}}_2 = -\hat{\mathbf{n}}_1$, the relation between tangential currents is

$$\mathbf{M}_1 = -\mathbf{M}_2 \quad (2.60)$$

$$\mathbf{J}_1 = -\mathbf{J}_2 \quad (2.61)$$

Integral equations can be solved together with Eqs. (2.60) and (2.61) to find the field everywhere.

Scattering by a perfect electric conductor

The case of a PEC scatterer is simpler than the general one. In a perfect conductor the internal field is known to be 0 everywhere, so we only need to solve for the outside field in V_1 . Furthermore, boundary condition (2.22) forces the tangential electric field to be 0 on S . This means that magnetic currents are not present on the surface

$$\left[\mathbf{E}_1^{\text{tot}} \right]_{\text{tan}} = \mathbf{0} \quad \longrightarrow \quad \mathbf{M}_1 = \mathbf{0} \quad (2.62)$$

Integral equations (2.54)–(2.57) in this case reduce to:

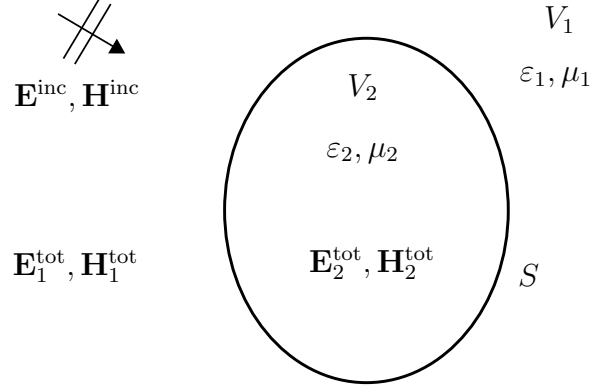
$$\left[\eta_1 \mathcal{L}_1[\mathbf{J}_1] \right]_{\text{tan}} = \left[\mathbf{E}^{\text{inc}} \right]_{\text{tan}} \quad (\text{T-EFIE}) \quad (2.63)$$

$$\left[\mathcal{K}_1^{\text{PV}}[\mathbf{J}_1] \right]_{\text{tan}} - \frac{1}{2} \hat{\mathbf{n}}_1 \times \mathbf{J}_1 = \left[\mathbf{H}^{\text{inc}} \right]_{\text{tan}} \quad (\text{T-MFIE}) \quad (2.64)$$

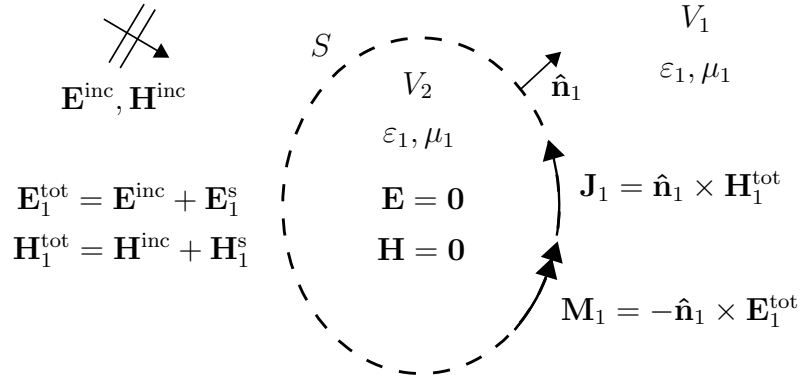
$$\hat{\mathbf{n}}_1 \times \eta_1 \mathcal{L}_1[\mathbf{J}_1] = \hat{\mathbf{n}}_1 \times \mathbf{E}^{\text{inc}} \quad (\text{N-EFIE}) \quad (2.65)$$

$$\hat{\mathbf{n}}_1 \times \mathcal{K}_1^{\text{PV}}[\mathbf{J}_1] + \frac{1}{2} \mathbf{J}_1 = \hat{\mathbf{n}}_1 \times \mathbf{H}^{\text{inc}} \quad (\text{N-MFIE}) \quad (2.66)$$

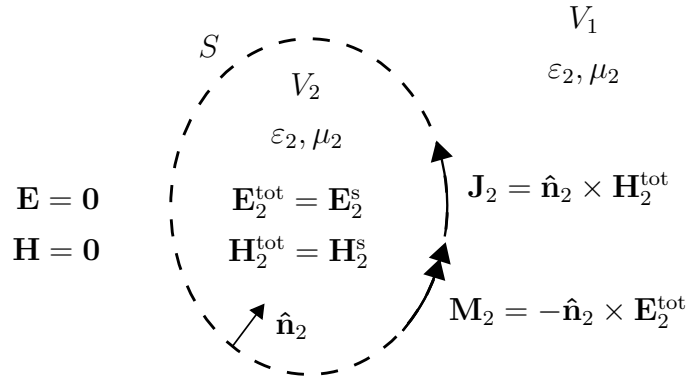
Only one of these equations need to be solved in order to find the unknown surface electric current \mathbf{J}_1 on S .



(a) Original scattering problem



(b) Equivalent problem in V_1



(c) Equivalent problem in V_2

Figure 2.1: Original and equivalent problems for scattering

2.3 Antenna parameters

Antenna performances can be evaluated with respect to a set of different parameters. The main ones are those related to input characteristics and far-field radiation. For aperture and low-profile antennas, also the *effective area* and beam efficiency play an important role in assessing the properties of the antenna. In this section, all parameters employed in the present work will be defined.

2.3.1 Input matching

From a circuit standpoint, the antenna can be represented as a passive load Z_{ant} . The resistive (real) part is related to the radiated and dissipated energy due to ohmic losses, while the reactive (imaginary) part is linked to the energy stored in the electromagnetic field.

$$Z_{\text{ant}} = R_{\text{rad}} + R_{\text{loss}} + jX_{\text{ant}} \quad (2.67)$$

the *radiation efficiency* can be expressed as:

$$\eta_R = \frac{R_{\text{rad}}}{R_{\text{rad}} + R_{\text{loss}}} \quad (2.68)$$

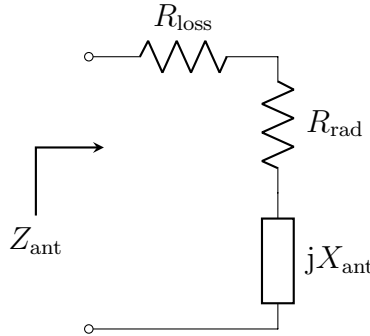


Figure 2.2: Antenna equivalent circuit

If the antenna is fed by a transmission line of characteristic impedance Z_0 , we can define an input reflection coefficient:

$$\Gamma_{\text{in}} = \frac{Z_{\text{ant}} - Z_0}{Z_{\text{ant}} + Z_0} \quad (2.69)$$

The input power can be written as:

$$P_{\text{in}} = P_{\text{av}} (1 - |\Gamma_{\text{in}}|^2) \quad (2.70)$$

where P_{av} is the available power from the generator, considered matched to the transmission line.

The objective is to provide the maximum power to the load, in this case the antenna, by making its input impedance equal to that of the feed line as much as possible. With this regard, the *Return Loss* is defined as:

$$\text{RL} = -20 \log_{10} |\Gamma_{\text{in}}| \quad (2.71)$$

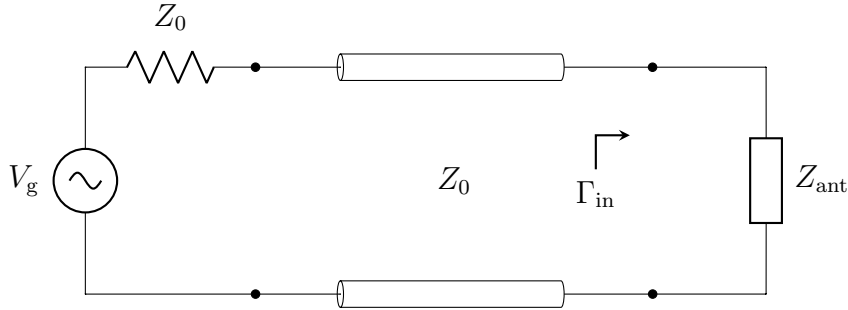


Figure 2.3: Antenna feeding schematic

2.3.2 Far-field radiation

The far-field radiation refers to the fields radiated by the antenna at a distance much larger than its dimensions and of the wavelength, where they can be approximated by a plane wave. The electric and magnetic fields can be computed easily from the current distribution on the surface of the antenna. Neglecting higher order terms, in far region they decay as $1/r$. For the vector potentials, we have [2]:

$$\mathbf{A}(\mathbf{r}) \xrightarrow{r \rightarrow \infty} \mu \frac{e^{-jkr}}{4\pi r} \int_{\mathcal{D}} \mathbf{J}(\mathbf{r}') e^{jk \hat{\mathbf{r}} \cdot \mathbf{r}'} d\mathcal{D}' \quad (2.72)$$

$$\mathbf{F}(\mathbf{r}) \xrightarrow{r \rightarrow \infty} \varepsilon \frac{e^{-jkr}}{4\pi r} \int_{\mathcal{D}} \mathbf{M}(\mathbf{r}') e^{jk \hat{\mathbf{r}} \cdot \mathbf{r}'} d\mathcal{D}' \quad (2.73)$$

Where the radiating currents are the impressed and equivalent ones in the outer volume. Plugging these in Eqs. (2.11) and (2.12) and neglecting higher order terms,

we get:

$$\mathbf{E}^{\text{far}}(\mathbf{r}) \approx -j\omega \left[(A_\theta + \eta F_\phi) \hat{\boldsymbol{\theta}} + (A_\phi - \eta F_\theta) \hat{\boldsymbol{\phi}} \right] \quad (2.74)$$

$$\mathbf{H}^{\text{far}}(\mathbf{r}) \approx -j\omega \left[\left(-\frac{1}{\eta} A_\phi + F_\theta \right) \hat{\boldsymbol{\theta}} + \left(\frac{1}{\eta} A_\theta + F_\phi \right) \hat{\boldsymbol{\phi}} \right] \quad (2.75)$$

The field has no radial component, since it decays faster than $1/r$ and is therefore negligible in far field.

One parameter of antennas related to the far-field is the *radiation intensity*, which is defined as the radiated power per unit solid angle:

$$I(\theta, \phi) = r^2 W_{\text{rad}} = r^2 \frac{1}{2\eta} (|E_\theta^{\text{far}}|^2 + |E_\phi^{\text{far}}|^2) \quad (2.76)$$

We can also define the *directivity* of an antenna, the ratio of radiation intensity with respect to an isotropic radiator that transmits the same power:

$$D(\theta, \phi) = \frac{4\pi}{P_{\text{rad}}} I(\theta, \phi) \quad (2.77)$$

Gain, instead, is defined as the ratio of radiation intensity with respect to input power, which takes into account ohmic losses:

$$G(\theta, \phi) = \frac{4\pi}{P_{\text{in}}} I(\theta, \phi) = \eta_R D(\theta, \phi) \quad (2.78)$$

Furthermore, the definition can include the input mismatch at antenna port by considering the available power of the generator, giving the *realized gain* [1]:

$$G_R(\theta, \phi) = \frac{4\pi}{P_{\text{av}}} I(\theta, \phi) = (1 - |\Gamma_{\text{in}}|^2) G(\theta, \phi) \quad (2.79)$$

where Γ_{in} is the reflection coefficient at the antenna input.

2.3.3 Effective area

The *effective area* is a quantity used to evaluate the radiation properties of the antenna with respect to its physical size. It is defined as the equivalent area that, when multiplied by the incident power density of a plane wave, gives the available power at the input terminals [2]. It is related to the directivity and is defined for its maximum value:

$$A_{\text{eff}} = \frac{\lambda^2}{4\pi} D_{\text{max}} \quad (2.80)$$

The effective area can be compared to the physical one, considered as the surface

on which the field radiates in free space, giving an *aperture efficiency*:

$$\eta_{\text{ap}} = \frac{A_{\text{eff}}}{A_{\text{geom}}} \quad (2.81)$$

It must be noted that Eq. (2.81) does not constitute a physical efficiency when applied to low-profile planar antennas, since the geometric area is usually taken to be the surface occupied by metallizations. Aperture efficiencies > 1 are possible for very directive antennas. Nonetheless, it remains a meaningful parameter to assess the geometrical efficiency.

2.3.4 Beam efficiency

In the context of directive antenna, an important parameter is the so called *beam efficiency*, which quantifies the fraction of power radiated within a cone of half-angle θ_1 compared to the total radiated power [2]. Considering an antenna with its main radiation direction along the z -axis, the beam efficiency can be calculated as:

$$\text{BE} = \frac{\int_0^{2\pi} \int_0^{\theta_1} I(\theta, \phi) \sin \theta d\theta d\phi}{\int_0^{2\pi} \int_0^{\pi} I(\theta, \phi) \sin \theta d\theta d\phi} \quad (2.82)$$

In reception, beam efficiency can be used to judge the ability of the antenna to discriminate between signals received through its main lobe and those from the minor lobes. High values are necessary for those applications where received signal from the minor lobes must be minimized, like in radar or astronomy.

A related quantity is the *Half-Power Beamwidth* (HPBW) which is defined as the angle between the two directions in which the radiation intensity is one-half of the maximum [1].

Chapter 3

Computational electromagnetics

In this chapter, the computational electromagnetics involved in the present work will be introduced briefly: in Sec. 3.1 the Method of Moments is formulated, then in Sec. 3.1.3 it is applied to EM radiation problems. Finally, source modeling and field calculation are discussed.

3.1 Method of Moments for electromagnetic simulation

In the field of computational electromagnetics (CEM), a range of simulation techniques are available for the solution of complicated problems, for which an analytical solution is not feasible. Between them, the *Method of Moments* [9, 8] is particularly suited to the treatment of scattering from homogeneous bodies. This is especially true for antenna design, where one is usually interested in the far field radiation.

By means of equivalence theorems presented in section 2.2.2, only the boundary of homogeneous bodies need to be discretized, not free space, and the solution will be in terms of equivalent electric and magnetic surface current densities which constitute the sources of the field. This allows a great reduction of the problem size with respect to other methods, namely *Finite Element* (FEM) and *Finite Difference* (FD), which require a discretization of the entire solution domain.

Furthermore, the radiation condition at infinity is automatically satisfied by the use of analytical Green's function, and the space need not be artificially terminated as in other methods. This is also true for planar multilayer and periodic structures.

In the following, the general formulation of the electromagnetic problem will be outlined, then the Method of Moments will be used to obtain an approximate solution.

3.1.1 Method of Moments formulation

The general Method of Moments formulation [9] allows to solve integro-differential (linear) equations. The problem can be formulated as that of determining the unknown source term f due to excitation g :

$$\mathcal{L}[f] = g \quad (3.1)$$

where the linear operator \mathcal{L} describes the specific problem.

The first step toward the solution consists of expanding f into a combination of *basis functions*:

$$\tilde{f} = \sum_{n=1}^N a_n f_n \quad (3.2)$$

where \tilde{f} is the approximation of f in the space spanned by the basis functions. Since the accuracy of the algorithm depends greatly on the ability of the basis functions to represent the actual solution, they must be chosen depending on the problem and must belong to the domain of operator \mathcal{L} .

Substituting Eq. (3.2) in (3.1), and using the linearity of \mathcal{L} we can write:

$$\sum_{n=1}^N a_n \mathcal{L}[f_n] = g \quad (3.3)$$

The problem is reduced to the determination of coefficients a_n . The residue of the solution is given by:

$$R = \sum_{n=1}^N a_n \mathcal{L}[f_n] - g \quad (3.4)$$

We then need to introduce a suitable *inner product* defined as:

$$\langle f, w \rangle = \int_{\mathcal{D}} f \cdot w \, d\mathcal{D} \quad (3.5)$$

which is clearly symmetric and satisfies linearity conditions. The domain \mathcal{D} represents the range of operator \mathcal{L} and can be a curve, a surface or a volume.

In order to obtain a linear system of N equations from (3.3), we define a set of N linearly independent *testing functions* w_m in the range of \mathcal{L} . The residue (3.4) is then projected onto each of the testing functions, forcing it to be orthogonal to them:

$$\langle w_m, R \rangle = \left\langle w_m, \sum_{n=1}^N a_n \mathcal{L}[f_n] - g \right\rangle = 0 \quad m = 1, \dots, N$$

$$\sum_{n=1}^N a_n \langle w_m, \mathcal{L}[f_n] \rangle = \langle w_m, g \rangle \quad m = 1, \dots, N \quad (3.6)$$

Eq. (3.6) can be written in matrix form as:

$$\mathbf{L} \mathbf{a} = \mathbf{b} \quad (3.7)$$

where

$$\mathbf{L} = \begin{bmatrix} \langle w_1, \mathcal{L}[f_1] \rangle & \langle w_1, \mathcal{L}[f_2] \rangle & \cdots & \langle w_1, \mathcal{L}[f_N] \rangle \\ \langle w_2, \mathcal{L}[f_1] \rangle & \langle w_2, \mathcal{L}[f_2] \rangle & \cdots & \langle w_2, \mathcal{L}[f_N] \rangle \\ \vdots & \vdots & \ddots & \vdots \\ \langle w_N, \mathcal{L}[f_1] \rangle & \langle w_N, \mathcal{L}[f_2] \rangle & \cdots & \langle w_N, \mathcal{L}[f_N] \rangle \end{bmatrix}$$

$$\mathbf{a} = \begin{bmatrix} a_1 \\ a_2 \\ \vdots \\ a_N \end{bmatrix} \quad \mathbf{b} = \begin{bmatrix} \langle w_1, g \rangle \\ \langle w_2, g \rangle \\ \vdots \\ \langle w_N, g \rangle \end{bmatrix}$$

The linear system (3.7) can then be solved by means of direct or iterative solvers. The choice can be influenced by matrix properties, which in turn depend on the chosen basis functions.

The case where the basis and testing function coincide ($w_n = f_n$) is known as *Galerkin's method*.

3.1.2 Basis functions

In the treatment of scatterer in 3D space, it is useful to discretize boundaries by subdividing them into planar triangular patches. This option allows to mesh arbitrary continuous surfaces. The higher the number of patches, the better the algorithm resolution.

Once meshed, a number of *local* basis functions are assigned on the surface. One particular choice is that of Rao-Wilton-Glisson (RWG) functions [15], which are defined on couples of triangles sharing an edge. A function \mathbf{f}_n assigned to edge

e_n , shared by triangles T_n^+ and T_n^- , is defined as

$$\mathbf{f}_n(\mathbf{r}) = \begin{cases} \frac{l_n}{2A_n^+} (\mathbf{r} - \mathbf{p}_n^+) & \mathbf{r} \in T_n^+ \\ \frac{l_n}{2A_n^-} (\mathbf{p}_n^- - \mathbf{r}) & \mathbf{r} \in T_n^- \\ 0 & \text{otherwise} \end{cases} \quad (3.8)$$

Here A_n^\pm are the areas of triangle T_n^\pm , l_n is the length of the common edge e_n and \mathbf{p}_n^\pm are the “free” vertex of T_n^\pm as represented in fig. 3.1.

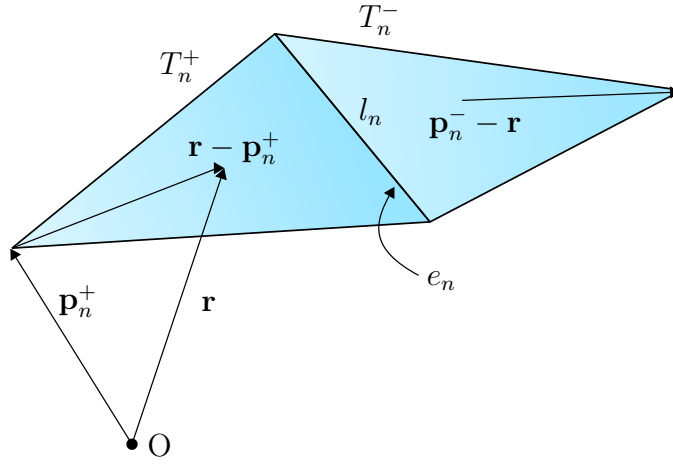


Figure 3.1: RWG function \mathbf{f}_n assigned on the edge e_n

One important property of these basis function is that its curl is constant and opposite on the two triangles that form its support.

$$\nabla \cdot \mathbf{f}_n(\mathbf{r}) = \begin{cases} \frac{l_n}{2A_n^+} & \mathbf{r} \in T_n^+ \\ -\frac{l_n}{2A_n^-} & \mathbf{r} \in T_n^- \\ 0 & \text{otherwise} \end{cases} \quad (3.9)$$

When used to represent the surface current density \mathbf{J}_s , their divergence is proportional to the surface charge density through the continuity equations (2.5) and (2.6). This means that the sum of surface charges on both side will be zero, avoiding the accumulation of spurious charges on the edge. For this reason, RWG functions are said to be *divergence conforming*.

3.1.3 Discretization by Galerkin’s method and RWG basis functions

The *Method of Moments* discussed in Sec. 3.1 can be readily applied to solve the integral equation derived in Sec. 2.2.2. RWG functions are used to discretize the current density \mathbf{J} on the surface of objects:

$$\mathbf{J}(\mathbf{r}) = \sum_{n=1}^N J_n \mathbf{f}_n(\mathbf{r}) \quad (3.10)$$

The same basis functions are used for the magnetic current \mathbf{M} :

$$\mathbf{M}(\mathbf{r}) = \sum_{n=1}^N M_n \mathbf{f}_n(\mathbf{r}) \quad (3.11)$$

With these expansions, we can rewrite Eqs. (2.56) and (2.57) in terms of unknown coefficients J_n and M_n :

$$\sum_{n=1}^N J_n \left(\hat{\mathbf{n}} \times \eta \mathcal{L}[\mathbf{f}_n] \right) - \sum_{n=1}^N M_n \left(\hat{\mathbf{n}} \times \mathcal{K}^{\text{PV}}[\mathbf{f}_n] + \frac{1}{2} \mathbf{f}_n \right) = \hat{\mathbf{n}} \times \mathbf{E}^{\text{inc}} \quad (3.12)$$

$$\sum_{n=1}^N J_n \left(\hat{\mathbf{n}} \times \mathcal{K}^{\text{PV}}[\mathbf{f}_n] + \frac{1}{2} \mathbf{f}_n \right) + \sum_{n=1}^N M_n \left(\hat{\mathbf{n}} \times \frac{1}{\eta} \mathcal{L}[\mathbf{f}_n] \right) = \hat{\mathbf{n}} \times \mathbf{H}^{\text{inc}} \quad (3.13)$$

Of course, these two equations cannot be solved since there are $2N$ unknowns. Following the Galerkin’s testing procedure described in Sec. 3.1, we proceed to test each equation against all the basis functions, with the inner product defined in (3.5):

$$\sum_{n=1}^N J_n \eta \left\langle \mathbf{f}_m, \hat{\mathbf{n}} \times \mathcal{L}[\mathbf{f}_n] \right\rangle - \sum_{n=1}^N M_n \left\langle \mathbf{f}_m, \hat{\mathbf{n}} \times \mathcal{K}^{\text{PV}}[\mathbf{f}_n] + \frac{1}{2} \mathbf{f}_n \right\rangle = \left\langle \mathbf{f}_m, \hat{\mathbf{n}} \times \mathbf{E}^{\text{inc}} \right\rangle \quad (3.14)$$

$$\sum_{n=1}^N J_n \left\langle \mathbf{f}_m, \hat{\mathbf{n}} \times \mathcal{K}^{\text{PV}}[\mathbf{f}_n] + \frac{1}{2} \mathbf{f}_n \right\rangle + \sum_{n=1}^N M_n \frac{1}{\eta} \left\langle \mathbf{f}_m, \hat{\mathbf{n}} \times \mathcal{L}[\mathbf{f}_n] \right\rangle = \left\langle \mathbf{f}_m, \hat{\mathbf{n}} \times \mathbf{H}^{\text{inc}} \right\rangle \quad (3.15)$$

Defining:

$$\begin{aligned}
 A_{mn} &= \left\langle \mathbf{f}_m, \hat{\mathbf{n}} \times \mathcal{L}[\mathbf{f}_n] \right\rangle \\
 B_{mn} &= \left\langle \mathbf{f}_m, \hat{\mathbf{n}} \times \mathcal{K}^{\text{PV}}[\mathbf{f}_n] \right\rangle \\
 I_{mn} &= \left\langle \mathbf{f}_m, \mathbf{f}_n \right\rangle \\
 V_m^E &= \left\langle \mathbf{f}_m, \hat{\mathbf{n}} \times \mathbf{E}^{\text{inc}} \right\rangle \\
 V_m^H &= \left\langle \mathbf{f}_m, \hat{\mathbf{n}} \times \mathbf{H}^{\text{inc}} \right\rangle
 \end{aligned}$$

we can express Eqs. (3.14) and (3.15) in matrix notation as:

$$\begin{bmatrix} \mathbf{Z}^{EJ} & \mathbf{Z}^{EM} \\ \mathbf{Z}^{HJ} & \mathbf{Z}^{HM} \end{bmatrix} \begin{bmatrix} \mathbf{J} \\ \mathbf{M} \end{bmatrix} = \begin{bmatrix} \mathbf{V}^E \\ \mathbf{V}^H \end{bmatrix} \quad (3.16)$$

where:

$$\begin{bmatrix} \mathbf{Z}^{EJ} & \mathbf{Z}^{EM} \\ \mathbf{Z}^{HJ} & \mathbf{Z}^{HM} \end{bmatrix} = \begin{bmatrix} \eta \mathbf{A} & \mathbf{B} + \frac{1}{2} \mathbf{I} \\ \mathbf{B} + \frac{1}{2} \mathbf{I} & \frac{1}{\eta} \mathbf{A} \end{bmatrix} \quad (3.17)$$

Each entry Z_{ij} quantifies the interaction of the j -th source with the i -th function. Interactions are considered for each combination of electric and magnetic currents. The required integrals are calculated as follows:

$$\begin{aligned}
 A_{mn} &= jk \left[\iint_{\mathcal{S}_m} \mathbf{f}_m(\mathbf{r}) \cdot \hat{\mathbf{n}} \times \iint_{\mathcal{S}_n} \mathbf{f}_n(\mathbf{r}') \frac{e^{jkr}}{4\pi r} dS' dS \right. \\
 &\quad \left. + \frac{1}{k^2} \iint_{\mathcal{S}_m} \mathbf{f}_m(\mathbf{r}) \cdot \hat{\mathbf{n}} \times \nabla \iint_{\mathcal{S}_n} \nabla'_s \cdot \mathbf{f}_n(\mathbf{r}') \frac{e^{jkr}}{4\pi r} dS' dS \right] \quad (3.18)
 \end{aligned}$$

$$B_{mn} = \iint_{\mathcal{S}_m} \mathbf{f}_m(\mathbf{r}) \cdot \hat{\mathbf{n}} \times \iint_{\mathcal{S}_n} \mathbf{f}_n(\mathbf{r}') \times \left(jk + \frac{1}{r} \right) \frac{e^{jkr}}{4\pi r} \hat{\mathbf{r}} dS' dS \quad (3.19)$$

$$I_{mn} = \iint_{\mathcal{S}_m} \iint_{\mathcal{S}_n} \mathbf{f}_m(\mathbf{r}) \cdot \mathbf{f}_n(\mathbf{r}') dS' dS \quad (3.20)$$

$$V_m^E = \iint_{\mathcal{S}_m} \mathbf{f}_m(\mathbf{r}) \cdot \hat{\mathbf{n}} \times \mathbf{E}^{\text{inc}}(\mathbf{r}) dS \quad (3.21)$$

$$V_m^H = \iint_{\mathcal{S}_m} \mathbf{f}_m(\mathbf{r}) \cdot \hat{\mathbf{n}} \times \mathbf{H}^{\text{inc}}(\mathbf{r}) dS \quad (3.22)$$

where \mathcal{S}_m and \mathcal{S}_n are the support surfaces of functions \mathbf{f}_m and \mathbf{f}_n respectively. ∇'_s

indicates the surface divergence in primed coordinates.

Case of a dielectric

Referring to the problem of scattering by a dielectric object, analyzed in Sec. 2.2.2, the above discretization must be valid in both medium 1 and 2. In particular, we will have 2 sets of coefficients, one for each medium as indicated by the superscript:

$$\begin{aligned} \mathbf{J}_1 &= \sum_{n=1}^N J_n^{(1)} \mathbf{f}_n^{(1)} & \mathbf{M}_1 &= \sum_{n=1}^N M_n^{(1)} \mathbf{f}_n^{(1)} \\ \mathbf{J}_2 &= \sum_{n=1}^N J_n^{(2)} \mathbf{f}_n^{(2)} & \mathbf{M}_2 &= \sum_{n=1}^N M_n^{(2)} \mathbf{f}_n^{(2)} \end{aligned}$$

By a convenient placement of basis functions on both sides, we can easily enforce the continuity boundary condition for the field (Eqs. (2.61) and (2.60)). In particular, if the function on side 1 is opposite to that of side 2, the unknown coefficient will be equal [21]:

$$\mathbf{f}_n^{(1)} = -\mathbf{f}_n^{(2)} = \mathbf{f}_n \quad \longrightarrow \quad J_n^{(1)} = J_n^{(2)} = J_n, \quad M_n^{(1)} = M_n^{(2)} = M_n \quad (3.23)$$

therefore, we can drop the superscript for the unknown coefficients. The system matrix for both sides can be computed as:

$$A_{mn}^{(1)} = \langle \mathbf{f}_m, \hat{\mathbf{n}} \times \mathcal{L}_1[\mathbf{f}_n] \rangle \quad A_{mn}^{(2)} = -\langle \mathbf{f}_m, \hat{\mathbf{n}} \times \mathcal{L}_2[\mathbf{f}_n] \rangle \quad (3.24)$$

$$B_{mn}^{(1)} = \langle \mathbf{f}_m, \hat{\mathbf{n}} \times \mathcal{K}_1^{\text{PV}}[\mathbf{f}_n] \rangle \quad B_{mn}^{(2)} = -\langle \mathbf{f}_m, \hat{\mathbf{n}} \times \mathcal{K}_2^{\text{PV}}[\mathbf{f}_n] \rangle \quad (3.25)$$

$$I_{mn}^{(1)} = \langle \mathbf{f}_m, \mathbf{f}_n \rangle \quad I_{mn}^{(2)} = \langle \mathbf{f}_m, \mathbf{f}_n \rangle \quad (3.26)$$

and

$$\begin{aligned} \mathbf{V}^{E(2)} &= \mathbf{0} \\ \mathbf{V}^{H(2)} &= \mathbf{0} \end{aligned}$$

since the incident field is zero inside region 2. The system to be solved is obtained by combining matrices of the type (3.16) for both regions:

$$\begin{bmatrix} \eta_1 \mathbf{A}^{(1)} + \eta_2 \mathbf{A}^{(2)} & \mathbf{B}^{(1)} + \mathbf{B}^{(2)} + \mathbf{I} \\ \mathbf{B}^{(1)} + \mathbf{B}^{(2)} + \mathbf{I} & \frac{1}{\eta_1} \mathbf{A}^{(1)} + \frac{1}{\eta_2} \mathbf{A}^{(2)} \end{bmatrix} \begin{bmatrix} \mathbf{J} \\ \mathbf{M} \end{bmatrix} = \begin{bmatrix} \mathbf{V}^{E(1)} \\ \mathbf{V}^{H(1)} \end{bmatrix} \quad (3.27)$$

Once solved, the currents in both regions can be recovered by multiplying the coefficients by corresponding basis functions.

Case of a PEC

The case of a PEC surface is much simpler. In fact, the field inside the surface is null, thus also the internal currents are zero on the inner surface; moreover, the magnetic currents are not present on the outer surface due to boundary condition (2.62). The unknowns are only the electric current coefficients for the outer region, and the system reduces to:

$$[\mathbf{Z}^{EJ}] [\mathbf{J}] = [\mathbf{V}^E] \quad (3.28)$$

Case of a PEC on a junction between two dielectric domains

A particular case is that of a junction of two dielectric domains where part, but not all, of the surface is covered by a perfect electric conductor. The field penetrates inside the volume. On the junction of the two pure dielectric domains, the situation is analogous to that already discussed, with the continuity of electric and magnetic currents:

$$\mathbf{f}_n \text{ on dielectric} \quad \longrightarrow \quad J_n^{(1)} = J_n^{(2)}, \quad M_n^{(1)} = M_n^{(2)}$$

On the PEC, magnetic currents cannot be present, therefore their coefficients must be zero. At the same time, electric currents on both sides are allowed to radiate independently in their respective medium, so their coefficients can be different:

$$\mathbf{f}_n \text{ on PEC} \quad \longrightarrow \quad J_n^{(1)} \neq J_n^{(2)}, \quad M_n^{(1)} = M_n^{(2)} = 0$$

In the assembly of the system matrix, it is useful to split the coefficients of the currents on the dielectric junction (\mathbf{J}_d and \mathbf{M}_d) and of those on the PEC (\mathbf{J}_m). With this convention, the matrix can be written as:

$$\begin{bmatrix} \mathbf{Z}_{dd}^{EJ} & \mathbf{Z}_{dd}^{EM} & \mathbf{Z}_{dm}^{EJ} \\ \mathbf{Z}_{dd}^{HJ} & \mathbf{Z}_{dd}^{HM} & \mathbf{Z}_{dm}^{HJ} \\ \mathbf{Z}_{md}^{EJ} & \mathbf{Z}_{md}^{EM} & \mathbf{Z}_{mm}^{EJ} \end{bmatrix} \begin{bmatrix} \mathbf{J}_d \\ \mathbf{M}_d \\ \mathbf{J}_m \end{bmatrix} = \begin{bmatrix} \mathbf{V}_d^E \\ \mathbf{V}_d^H \\ \mathbf{V}_m^E \end{bmatrix} \quad (3.29)$$

where the subscript d stands for *dielectric*, while m stands for *metal*.

It is worth noting that the total number of coefficients is still equal to $2N$ (where N is the number of basis functions) because, referring to a function on the PEC, we have one less coefficient due to the absence of magnetic current, but we have two independent coefficients, instead of one, for the electric currents on both sides.

Functions that lie on the boundary of the PEC surface must be treated carefully: on the triangle that lies on the conductor, magnetic current are not allowed, while on the other triangle boundary conditions impose the equality of electric currents on both sides. This means that, for these functions, there is only one associated coefficient which is that of electric currents on dielectric [19].

3.1.4 Source modeling

The solution of an electromagnetic problem requires the definition of a source (forcing term). In the case of scattering, the incident field is usually defined as a plane wave impinging on the structure. For antenna radiation, instead, the incident field is expressed in terms of lumped port voltage. In the so called *Delta-gap model* [8], a potential difference is considered applied to two infinitesimally close edges (Fig. 3.2). If we take the limit of the applied electric field for the gap approaching 0 length, it can be represented as a Dirac delta source on the edge in the direction normal to it:

$$\mathbf{E}^{\text{inc}} = V_{\text{in}} \delta(\mathbf{r}) \hat{\mathbf{n}}_m \quad \mathbf{r} \in e_m \quad (3.30)$$

where $\hat{\mathbf{n}}_m$ is the normal unit vector to edge e_m . Since the basis function has a unity normal component along the edge, the integral becomes simply the product of the voltage times the length of the edge:

$$V_m^E = \langle \mathbf{f}_m, \mathbf{E}^{\text{inc}} \rangle = \iint_{S_m} \mathbf{f}_m(\mathbf{r}) \cdot V_{\text{in}} \delta(\mathbf{r}) \hat{\mathbf{n}}_m dS = \pm V_{\text{in}} l_m \quad (3.31)$$

the + sign is when the direction of the function is coherent with the applied voltage, the – sign when they are opposite. In this way, the construction of the RHS of the system is greatly simplified. The current flowing through edge e_m can be calculated

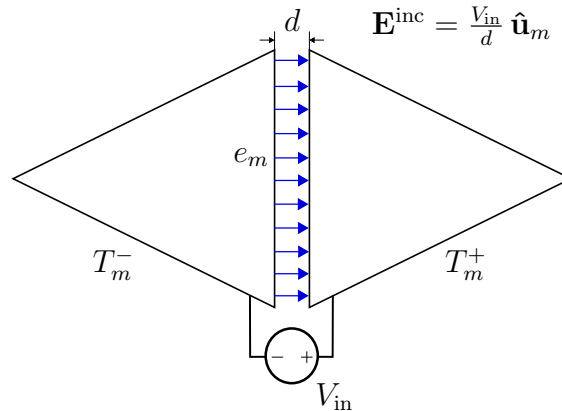


Figure 3.2: *Delta-gap* feed model

taking into account the basis expansion (3.10) and it is equal to the basis coefficient

multiplied by the edge length:

$$I_m = \int_{e_m} \mathbf{J} \cdot \hat{\mathbf{n}}_m dl = J_m \int_{e_m} \mathbf{f}_m \cdot \hat{\mathbf{n}}_m dl = \pm J_m l_m \quad (3.32)$$

since, along the edge, the component of the basis function normal to it is always unitary. The sign takes into account the orientation of function with respect to reference direction of the current.

Finally, the input impedance can be calculated as the ratio of the applied voltage to the current as:

$$Z_{\text{in}} = \frac{V_{\text{in}}}{I_m} = \frac{V_{\text{in}}}{a_m l_m} \quad (3.33)$$

In case the port spans more than one function, the total current will be the sum of currents flowing through each edge.

3.2 Analysis of multiport structures

The analysis of multiport electromagnetic structures is tackled by reducing the problem from a three-dimensional one to a one-dimensional circuit equivalent. In particular, a solution is obtained by exciting one port at a time with a known voltage, with the others short-circuited. This allows to extract the admittance matrix of the structure seen as a multiport device:

$$\begin{bmatrix} I_1 \\ \vdots \\ I_N \end{bmatrix} = \begin{bmatrix} Y_{11} & \dots & Y_{1N} \\ \vdots & \ddots & \vdots \\ Y_{N1} & \dots & Y_{NN} \end{bmatrix} \begin{bmatrix} V_1 \\ \vdots \\ V_N \end{bmatrix} \quad (3.34)$$

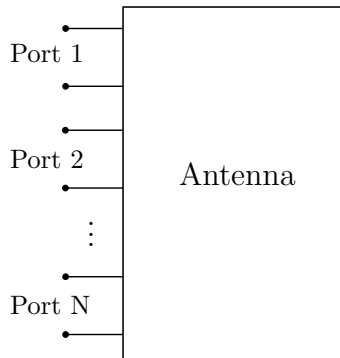


Figure 3.3: Antenna as a multiport equivalent circuit

In the case of reconfigurable antennas, one port is usually considered as the

input, while others represent switches that can be either open or closed depending on their impedance value. From this, a number of possible combinations can be simulated by closing each port with the corresponding impedance, and calculating the current flowing through them. Considering the admittance matrix, we have:

$$\begin{cases} \mathbf{I} = \mathbf{Y} \mathbf{V} \\ \mathbf{V} = \mathbf{V}_{\text{in}} - \mathbf{Z}_{\text{sw}} \mathbf{I} \end{cases} \quad (3.35)$$

where \mathbf{Z}_{sw} is the diagonal matrix representing switch impedances at each port. This system can be solved for the port voltages

$$\mathbf{V} = (\mathbf{1} + \mathbf{Z}_{\text{sw}} \mathbf{Y})^{-1} \mathbf{V}_{\text{in}} \quad (3.36)$$

The total current coefficients are recovered by the superposition of those produced by each port alone, weighted by the voltage amplitude measured at the input:

$$\begin{bmatrix} J_1^{\text{tot}} \\ J_2^{\text{tot}} \\ \vdots \\ J_N^{\text{tot}} \end{bmatrix} = V_1 \begin{bmatrix} J_{1,1} \\ J_{2,1} \\ \vdots \\ J_{N,1} \end{bmatrix} + V_2 \begin{bmatrix} J_{1,2} \\ J_{2,2} \\ \vdots \\ J_{N,2} \end{bmatrix} + \dots + V_N \begin{bmatrix} J_{1,N} \\ J_{2,N} \\ \vdots \\ J_{N,N} \end{bmatrix} \quad (3.37)$$

With this technique, an exhaustive search can be obtained by computing the equivalent circuit, then testing all possible switch configurations and looking at the resulting output (far field, reflection coefficient, etc.).

3.3 Far Field calculation

Once the coefficients of basis function are obtained, the antenna far field radiation can be calculated easily using Eqs. (2.74) and (2.75). These requires the integration of surface currents on each triangle to obtain vector potentials \mathbf{A} and \mathbf{F} . A sufficiently accurate estimate of the pattern can be achieved by approximating the surface integral for each function with the value that it possess at the centroid of the cell, multiplied by its area:

$$\begin{aligned} \mathbf{A}(\mathbf{r}) &= \mu \frac{e^{-jkr}}{4\pi r} \iint_{\mathcal{S}} \mathbf{J}(\mathbf{r}') e^{jk \hat{\mathbf{r}} \cdot \mathbf{r}'} dS' \\ &\approx \mu \frac{e^{-jkr}}{4\pi r} \sum_{i=1}^{N_{\text{cell}}} \mathbf{J}(\mathbf{r}_i^c) e^{jk \hat{\mathbf{r}} \cdot \mathbf{r}_i^c} \cdot \text{area}(\mathcal{S}_i) \end{aligned} \quad (3.38)$$

where \mathcal{S}_i indicates the i -th cell and \mathbf{r}_i^c is the position vector of its centroid. Depending on the cell position (internal, boundary or corner), the number of functions that are defined on it vary between 1 and 3. Each contribution must be summed to obtain the centroid value in Eq. (3.38).

The same can be done for the electric vector potential \mathbf{F} . Far field vectors are then recovered through Eqs. (2.74) and (2.75).

Chapter 4

Optimization techniques in antenna design

In this chapter, the algorithms employed for antenna optimization will be presented and the process adopted for this work will be outlined. In Sec. 4.1 Genetic algorithms are introduced, followed by a brief description of local optimization (Sec. 4.2). The combination of GA and MoM is discussed in Sec. 4.3.

4.1 Genetic algorithms

The optimization of antennas requires algorithms able to explore large solution spaces in a reasonable time, and to treat highly non-linear objective functions (this is the case for the mapping of antenna geometry to the parameters of interest, like input matching or far field radiation). Furthermore, this kind of problem are known as *unconstrained*, since constraints are not embedded in the algorithm; instead, unfeasible solutions are usually dealt with at a subsequent stage, by removing them from the solution set. With this regard, *Genetic algorithms* (GA) have been proven appropriate for a variety of electromagnetic design problems [18].

GA work by mimicking the evolutionary process found in nature, by which a population evolves based on the fitness of each individual. The main nature-derived features are [17]:

- the evolution is based on *chromosomes*, which are a coded representation of individuals, not on individuals themselves
- *selection* operates on individuals and decide which are more likely to reproduce based on their fitness
- evolution takes place during *reproduction*, when the recombination of genetic information from parents generates new individuals

- *mutation* ensures that the genetic variability is maintained throughout evolution
- the evolution process is memoryless, meaning that all information needed for reproduction is contained in the current generation of individuals.

GA differs from other traditional algorithms because it operates on a representation of the solution, called *chromosome*, and the optimization is carried out at population level, instead of single individuals, granting an inherent parallelism. This means that what is actually optimized is the *mean fitness* of the population, not the best individual overall. A suitable choice of parameters should allow good solutions to propagate quickly to subsequent generations, allowing a fast convergence of the algorithm.

The coding scheme defines the representation of solutions in the form of *chromosomes*. It is heavily dependent on the type of problem and may influence the algorithm efficiency. In most cases the solution is coded as a binary string, because they can be easily manipulated, although more sophisticated schemes can be useful to ease the decoding process or the definition of custom operators.

Given its characteristics, a few GA pros are:

- Ability to explore large solution spaces
- High flexibility due to its abstract implementation
- Ability to deal robustly with highly non-linear, stiff and non-differentiable objective functions
- Simultaneous exploration of several solutions due to its parallel nature
- Simplicity in the treatment of multi-objective optimization

4.1.1 Evolutionary operators

In this section, the operators involved in GA will be introduced and described in detail. They are:

- Selection
- Crossover (reproduction)
- Mutation
- Elite

Selection

The *selection* process picks individuals from the population based on their fitness value, which quantify their suitability in fulfilling the optimization goal.

The probability of an individual being selected can be related to its fitness value in two different ways, *roulette wheel* or *rank-based*. In the first case, the probability of each individual p_i is calculated as its fitness value f_i normalized to the sum of fitnesses of all individuals:

$$p_i = \frac{f_i}{\sum_{k=1}^N f_k} \quad (4.1)$$

where N is the population size. This is valid for maximization problems. In the minimization case, the scheme can be applied with a change of objective function through a linear transformation.

Rank-based selection sorts the individuals according to their fitness value. The probability is in this case proportional to the position of the individual in sorted order:

$$p_i = \frac{i}{\sum_{k=1}^N k} \quad f_{1,\dots,i-1} \leq f_i \leq f_{i+1,\dots,N} \quad (4.2)$$

The selection operator is the only one involving the objective function value and is therefore crucial in the convergence of the algorithm.

Crossover

The *crossover* operator is responsible for creating a new generation by hybridizing the genetic information of individuals chosen by the selection process. In the simplest case, two individuals a and b are randomly chosen and then coupled to create a new one. This coupling can be done in different ways, mainly *1-point* (also called *standard*), *2-point* or *uniform* crossover.

1-point crossover works by selecting a random location k along the chromosome length. The new chromosome is then assembled by combining genes of parent a from beginning to position k and those from parent b for the remaining part, as schematized in Fig. 4.1a.

2-point crossover is similar to the previous scheme, but this time two locations k_1, k_2 are chosen independently and the genes between positions k_1 and k_2 are taken from parent b , while those outside are taken from parent a (Fig. 4.1b).

In uniform crossover each gene of the new chromosome is inherited randomly from parent a or b with an equal probability (Fig. 4.1c).

Mutation

Mutation works on single chromosomes. Its operation consists in changing the content of a single gene randomly. This operator is applied only to a small set of individuals, controlled by the *mutation rate* parameter.

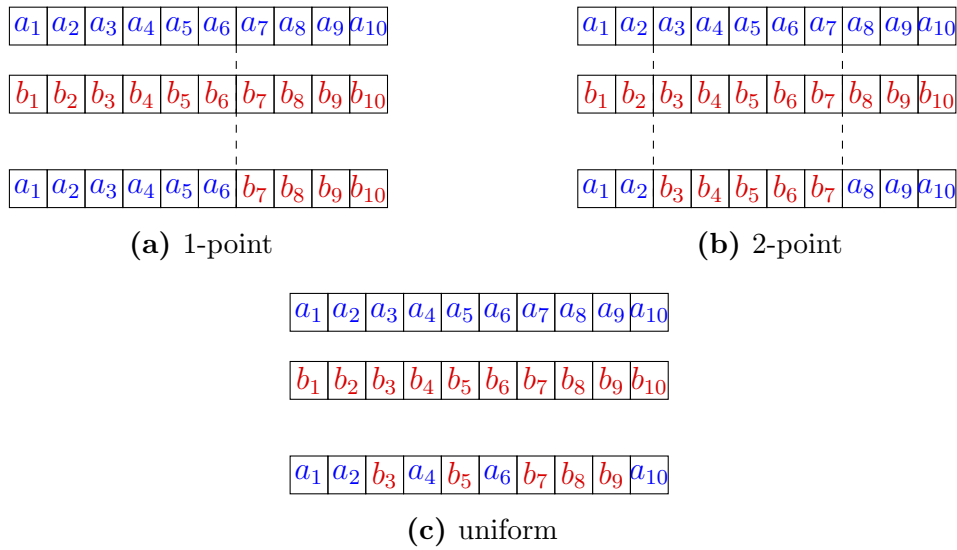


Figure 4.1: Different crossover operators

Mutation is vital in keeping the genetic variability needed to explore the solution space effectively. This avoids a possible stall of the algorithm due to the individuals being too similar after a number of iterations.

Elite

The *elite* operator propagates best individuals unmodified from one generation to the next. This is done to ensure that good chromosome do not get lost during the crossover and mutation phases. It is usually applied to a very small fraction of the population.

4.1.2 Optimization flow

Having listed all the operators involved in GA, the following step is the description of the process flow (as schematized in Fig. 4.2).

The first step requires the generation of a starting population, that is often completely random, although sometimes *a priori* knowledge of the chromosome coding can be used to start the algorithm with good individuals. This population is then evaluated through the fitness function, and the actual optimization loop starts.

First, *selection* defines a subset of individuals that will propagate their genetic information, then *crossover* generates a new population based on the coupling of these individuals. Finally, *mutation* acts on some of them by modifying their genes

randomly. After these stages, which embody the evolution process, the fitness of the resulting population is evaluated. If any of the stop criteria is met, the process ends, otherwise it starts all over again by acting on the present population. Stop criteria can include particular fitness values that are deemed sufficient for the task or a maximum number of generations.

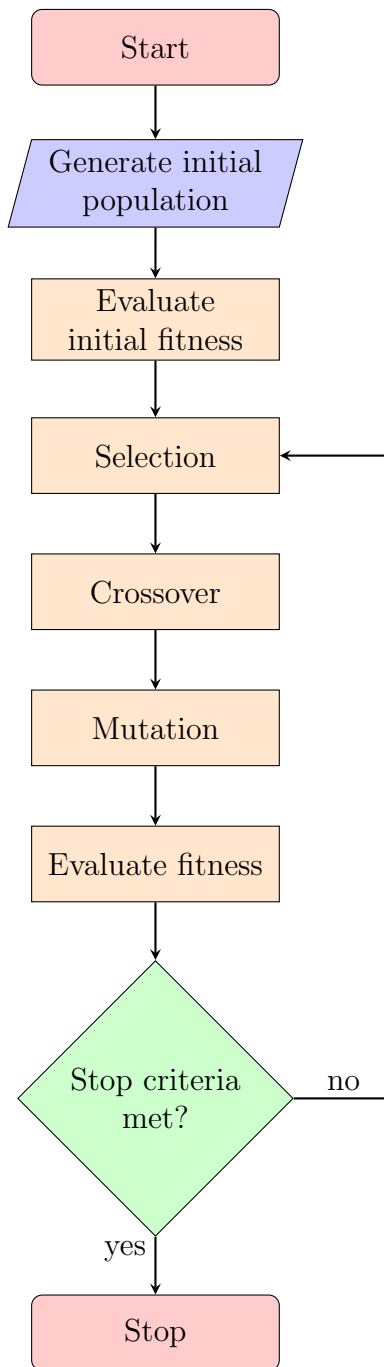


Figure 4.2: Flow diagram of Genetic Algorithm

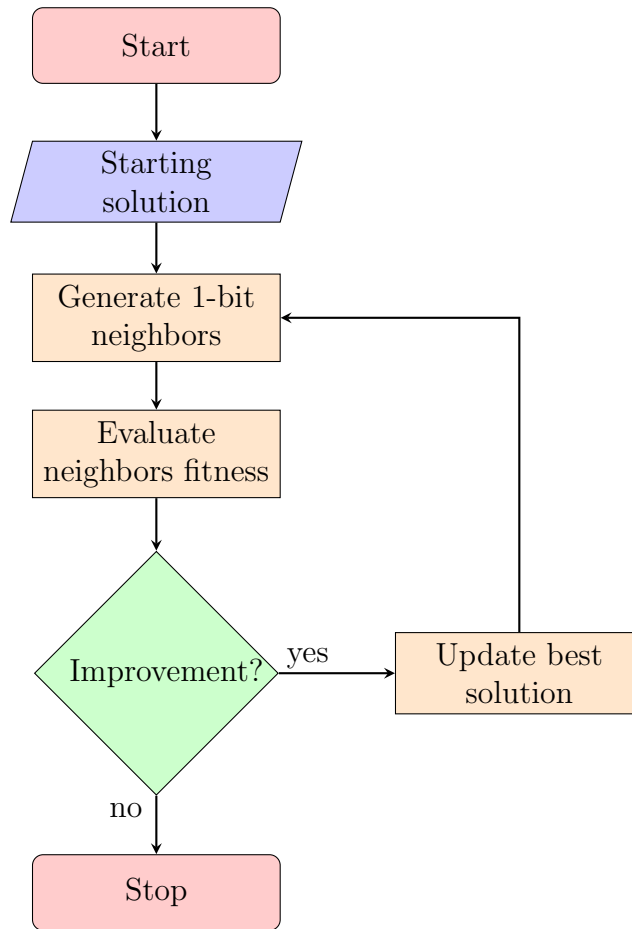


Figure 4.3: Flow diagram of 1-bit neighbor Local Optimizer

4.2 Local optimization

Since GA does not guarantee to converge to a minima of the objective function, it is customary to combine it with a local optimization algorithm. In fact, global optimization often stops in the surrounding of a local extrema, and a deterministic approach ensures the best possible outcome from a given starting point, which in this case is the output of GA.

It is also possible to embed local optimization inside the main GA loop (*Hybridization*): each newly generated chromosome is optimized locally before putting it into the next population.

Greedy 1-bit neighborhood search

In the context of local binary optimization, which deals with binary strings, one of the simplest algorithm is the *Greedy 1-bit neighborhood search* (Fig. 4.3). In particular, starting from the best solution obtained with the GA, the algorithm first generates all 1-bit neighbors (all the individuals obtained by flipping one bit at a time), then it evaluates them with the fitness function. If a better solution is found among them, the best solution is updated with this new chromosome and the local optimization cycle starts again until no further improvement is possible. This means that the output corresponds to a local minima.

4.3 GA and MoM for antenna design

In the simulation of antennas, the most computation intensive step is that involving the filling of the matrix arising from the application of MoM to the SIE. This dramatically limits the application of optimization algorithms, since even a slight modification of the antenna geometry usually requires the matrix to be recomputed completely or in part.

To avoid this problem, a solution is the combination of the Method of Moments with Genetic Algorithms (GA/MoM), introduced for the first time in [11], which allows to compute the structure matrix only once at the start of optimization process.

To illustrate the process, consider a structure composed of metal patches. Each independent portion is represented by a bit in the chromosome: a 1 means the presence of metal, while 0 means that it is removed. The \mathbf{Z} matrix is computed considering all metal portions that are allowed to be present, which constitute the so called “mother” structure (Fig. 4.4a). Setting a bit to 0 removes the corresponding portion, which is equivalent to forcing the current on it to be zero. This in turn means that the rows and columns of the \mathbf{Z} matrix involving the removed part will be filled with zeros (Fig. 4.4b).

In practice, setting entire rows and columns to zero makes the matrix singular. This is easily prevented by removing the required coefficients, creating the substructure matrix $\tilde{\mathbf{Z}}$. Accordingly, the corresponding current coefficients and forcing terms need to be deleted.

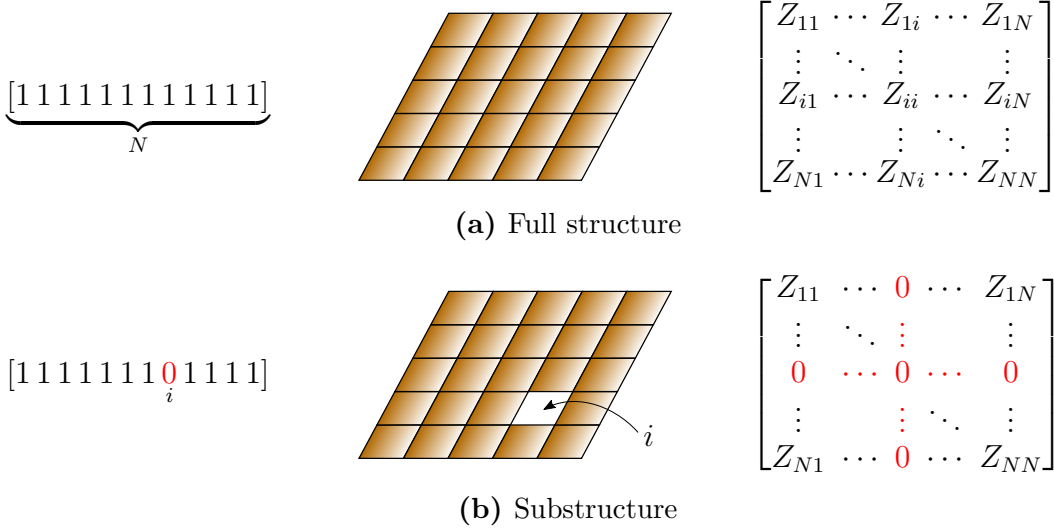


Figure 4.4: Comparison between “mother” structure (a) and a substructure obtained by removing one square (b): chromosome (left), geometry (center) and MoM matrix (right)

The linear system corresponding to the reduced structure will then be solved for the current coefficients. Currents are then mapped back to the original geometry and the parameters of interest (far field pattern, input impedance,...) can be calculated from them.

Since all the manipulations are done directly on the matrix, without referring to the geometry, this technique is called *Direct Matrix Manipulation* (DMM) and its flow is schematized in Fig. 4.5. In a GA algorithm, for each individual of the population, a different $\tilde{\mathbf{Z}}$ matrix is obtained and solved. Finally, the corresponding fitness value is calculated.

Matrix partitioning can also be used to further reduce computational cost, especially when the number of modifiable elements is less than or equal to that of fixed ones. Since this work deals with structure with a high degree of flexibility, this technique has not been implemented.

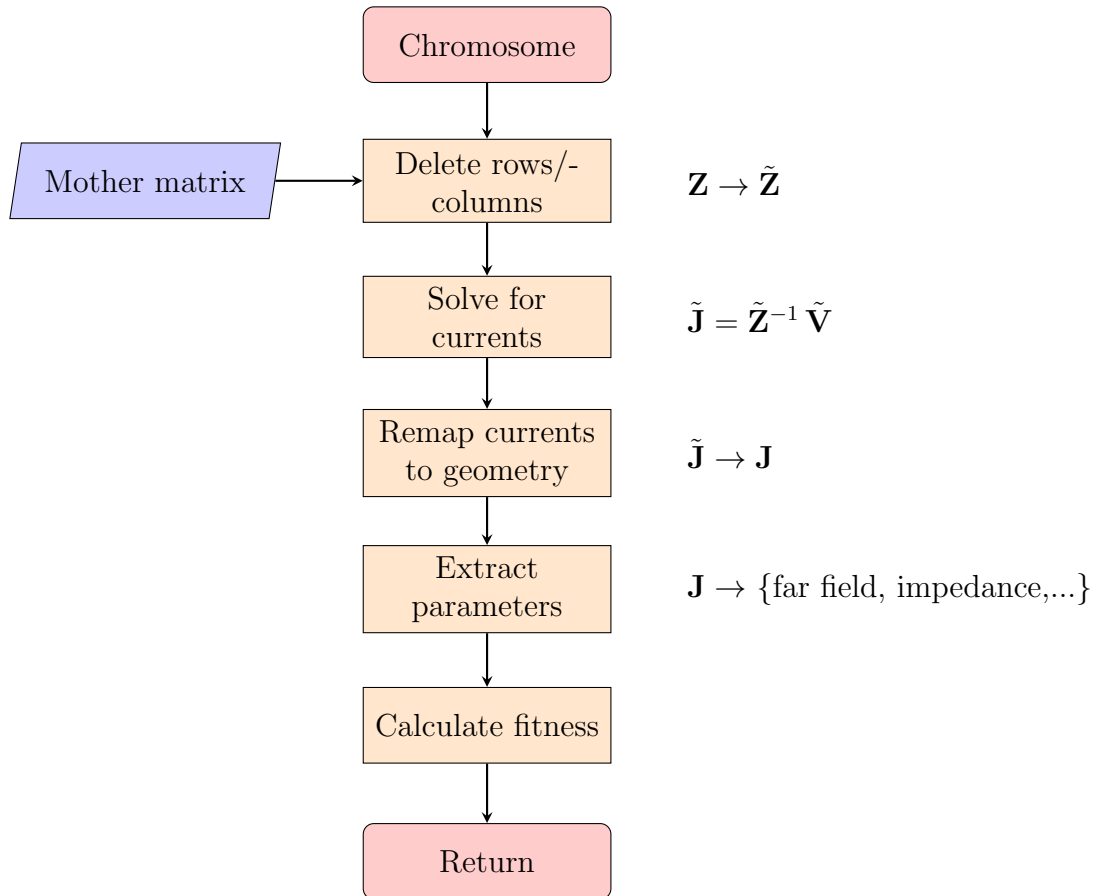


Figure 4.5: Flow diagram of Direct Matrix Manipulation for GA/MoM

Chapter 5

Optimization of low-profile directive antennas

The optimization of antennas with GA is introduced in [11]. Much of the present work originates from the code developed in [14] for the optimization of compact frequency-reconfigurable antennas. There, due to the complexity of the optimization process, the chromosome was rigidly mapped to the geometry mesh, with sectors defined as squares composed of two adjacent triangular cells, thereby not allowing a flexible choice of optimizable portions.

The requirements for optimization of directive antennas are different, since a finer mesh is needed for larger structures, rendering the problem size impractical if treated as in [14]. Therefore, the need to decouple the simulation mesh from the optimization arises.

The proposed approach exploits the flexibility offered by the preprocessor software GiD [5]. It allows the definition of custom properties useful to the optimization process, as well as an efficient meshing of the geometry. Then, the full structure is simulated with a MoM solver and the Z matrix is extracted. All these informations are gathered in Matlab for the optimization process. After that, the best design is validated with the help of commercial EM softwares (CST and FEKO). If all the criteria are met, it is finally prototyped and tested. This entire workflow is summarized in Fig. 5.1.

In case the required performances could not be met, this flow can be iterated, modifying the structure or the optimization mask accordingly.

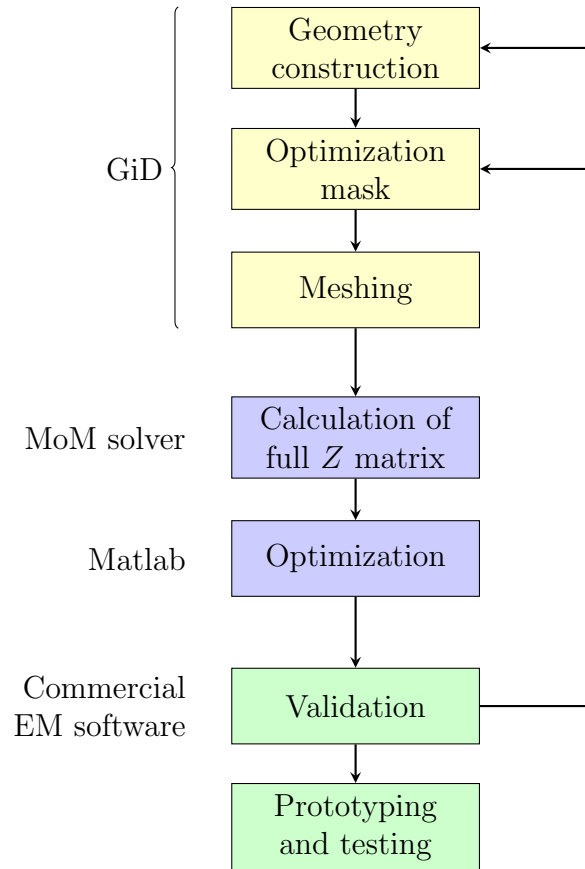


Figure 5.1: Proposed workflow for antenna optimization

5.1 Preprocessing

The preprocess stage starts with the construction of the full antenna geometry. Individual surfaces must be created for each independent optimizable sector, as shown in Fig. 5.2a.

For the optimization definitions, a custom *problem type* has been developed for GiD, which allows to assign a flag to specific geometry surfaces before meshing, defining which portions of the metal structure can be removed during optimization (Fig. 5.2b).

After that, the software runs through all the marked entities and assigns a progressive index that is mapped to the associated chromosome bit. Indexes can also be modified manually and the same index can be assigned to non-adjacent portions, providing more degrees of freedom to the designer. These values will be then transferred to each cell once the structure is meshed with the required resolution (Fig. 5.2c).

Having more optimizable surfaces means a larger solution space, which can help the convergence, but can also slow the process excessively. An acceptable trade-off must be found between speed and flexibility.

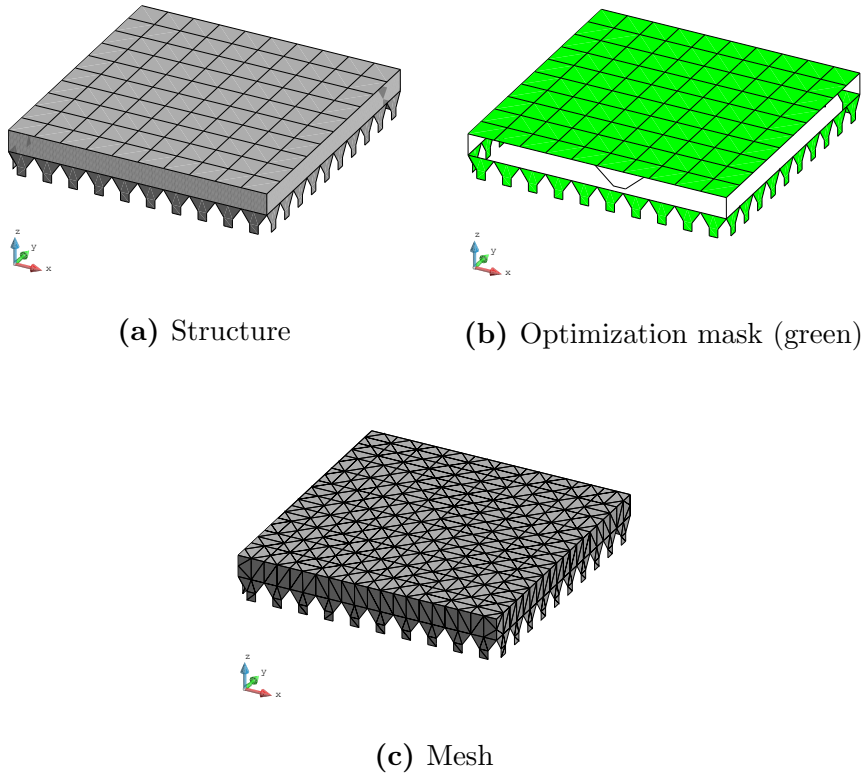


Figure 5.2: Example of geometry (a) with optimization mask (b) and corresponding mesh (c)

5.2 Matrix manipulation

Once the structure has been preprocessed and the Z matrix calculated, the optimization loop can start. This section is devoted to the step by step description of the manipulation required to obtain a substructure matrix from the full one. The case for metal structure is derived from [11], while the formulation for composite metal/dielectric structures has been developed from ground up during the present work.

5.2.1 Metal structures

The transition from a full matrix to the target submatrix for a metal-only structure is relatively straightforward. The crucial step in expanding the capabilities of the existent code is to map each optimizable cell onto the sector to whom it belongs, effectively decoupling the chromosome from the mesh (Fig. 5.3a). This information is then transferred to each basis function. All functions lying on edges inside a given sector are grouped (Fig. 5.3b), together with those lying on a boundary edge: this because the removal of a metal portion means that surface currents can no longer flow perpendicular to its boundary. Thus, these basis are not needed anymore to represent the current.

$$F_i = \{\mathbf{f}_n \mid e_n \in S_i\} \quad (5.1)$$

where S_i is the i -th sector. The function to be removed are then grouped together:

$$I_{\text{rem}} = \{i \mid g_i = 0\} \quad (5.2)$$

$$F_{\text{rem}} = \bigcup_{i \in I_{\text{rem}}} F_i \quad (5.3)$$

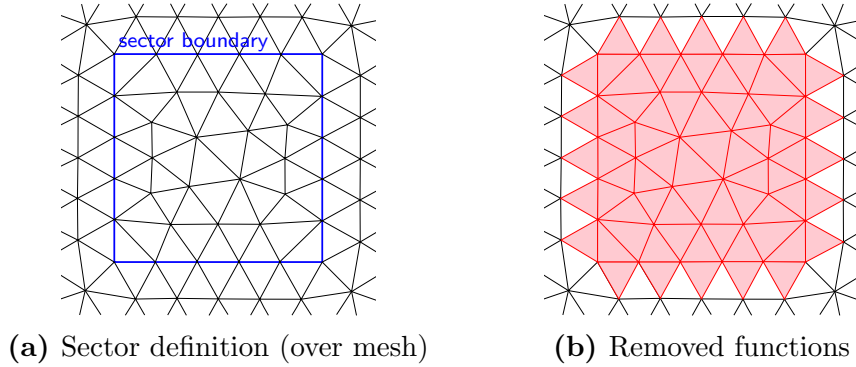


Figure 5.3: Sector definition (a) and functions that are cancelled when the sector is removed by the optimizer (b)

After this preliminary step, the procedure follows that described in Sec. 4.3: functions belonging to removed sectors are indexed and corresponding rows and columns of the matrix are discarded. This leaves the reduced Z matrix that can be solved to obtain input parameters and assess the performances of the antenna.

5.2.2 Composite metal/dielectric structures

The case for composite metal/dielectric structure is much more complicated, since there are many possible combinations. Before proceeding, all possible type of cells

are listed in Fig. 5.4, depending on mediums on both sides:

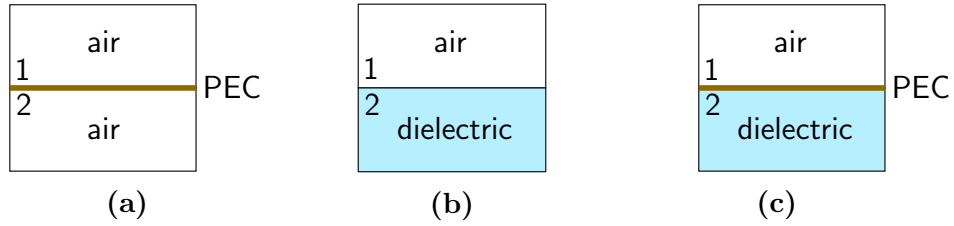


Figure 5.4: Possible cell types based on medium 1 and 2: PEC in air (a), boundary between air and dielectric (b) and PEC on a boundary between air and dielectric (c)

Each function is then categorized based on the nature of the two cells on which it is defined. A total of 4 combinations are possible, as shown in Fig. 5.5.

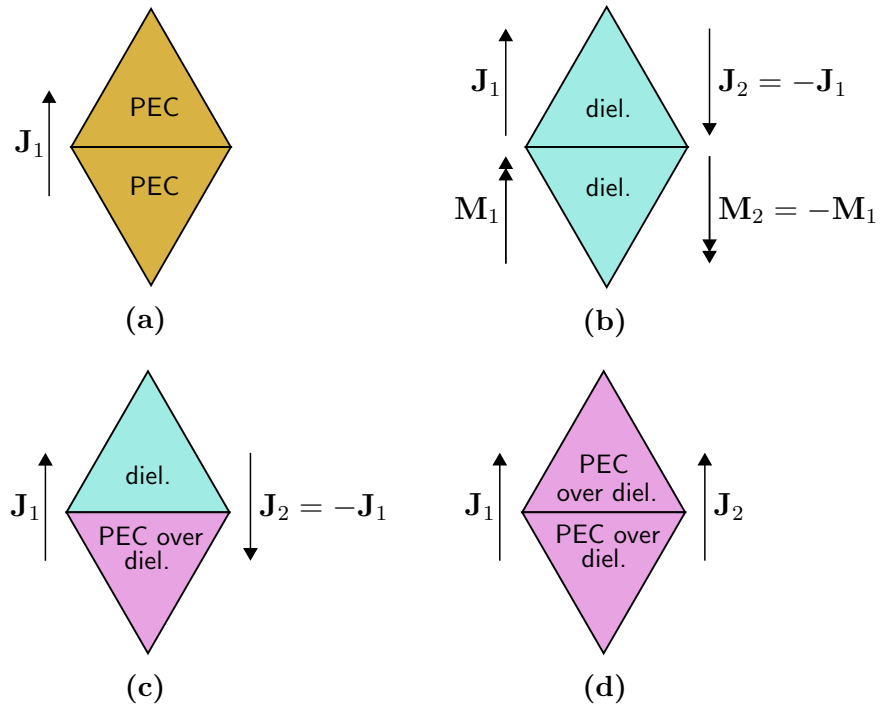


Figure 5.5: Possible function types with corresponding unknowns: PEC (a), dielectric (b), boundary between dielectric and PEC over dielectric (c) and PEC over dielectric (d)

For the optimization of metal/dielectric structures, it is essential to compute

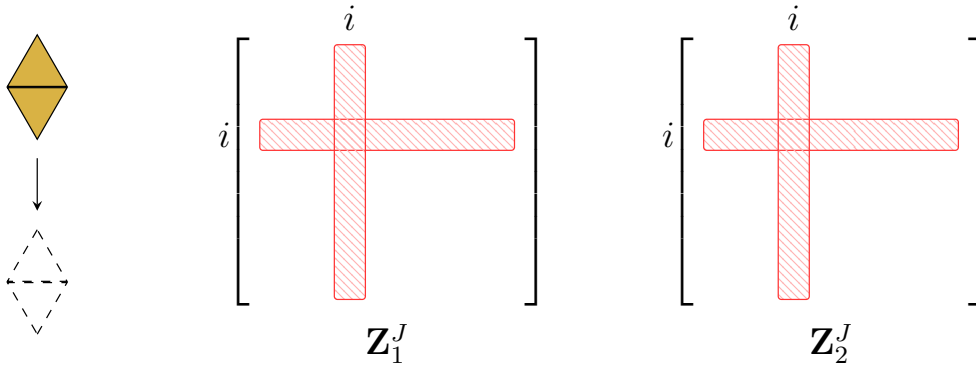
the Z matrices for the inner and outer region independently. Doing this allows to combine them in different ways during the optimization process. Depending on the required modification, these matrices are manipulated and then summed to obtain the complete linear system of Eq. (3.29).

During the structure definition, optimizable sectors are dealt with in different ways depending on their placement. For metal patches in air, the situation is analogous to the previously described one. Instead, when one wants to place an optimizable metal surface on a dielectric, the structure must be defined as a pure dielectric interface anyway. This because it is the case where all possible surface current coefficients are defined, allowing for any possible matrix modification.

The mapping of sectors is similar to the metal-only case. However, in presence of dielectrics, one needs to compute the cell modification first. Only after that, the resulting function is determined. This because multiple combinations are possible. Given how the algorithm is defined, only the addition of PEC is possible on a dielectric surface, reducing the total number of possibilities to just four. Depending on the original and modified function, all possible changes of the Z matrices are described.

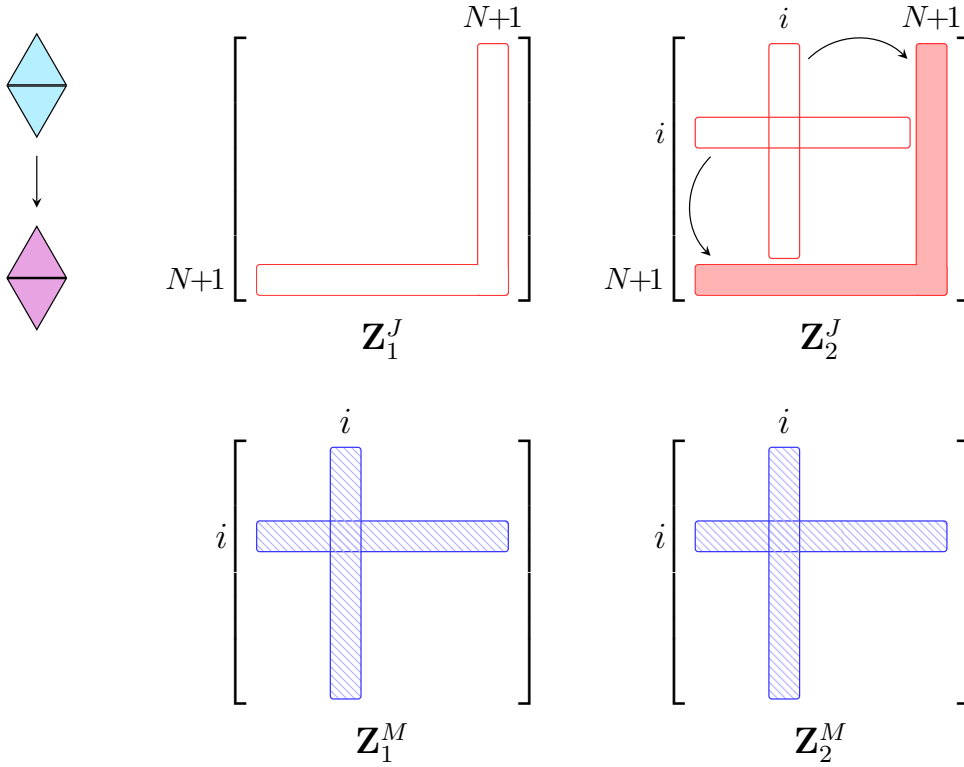
Removal of PEC on a function in air

This case is straightforward, and follows exactly the procedure outlined in Sec. 5.2.1. In fact, magnetic currents are not present, so only electric currents with their respective rows and columns need to be removed from the two Z matrices.



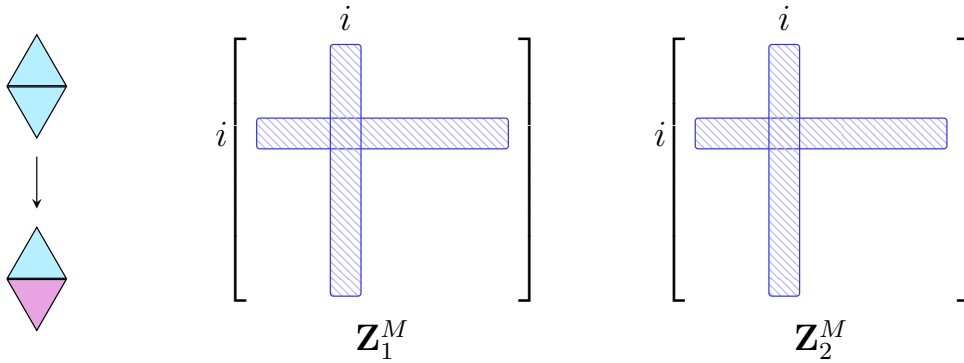
Addition of PEC on a dielectric function

The addition of PEC on a dielectric function removes the possibilities of magnetic current flowing on it, but at the same time it makes the electric currents on both sides independent of one another. Keeping in mind that the final system is given by the sum of the two matrices, this means that the rows and columns of matrix \mathbf{Z}_2^J linked to the i -th electrical function must be moved to a new position, leaving the old ones filled with zeros; meanwhile, matrix \mathbf{Z}_1^J is modified with new rows and columns to accommodate this change.



Addition of PEC on half of a dielectric function

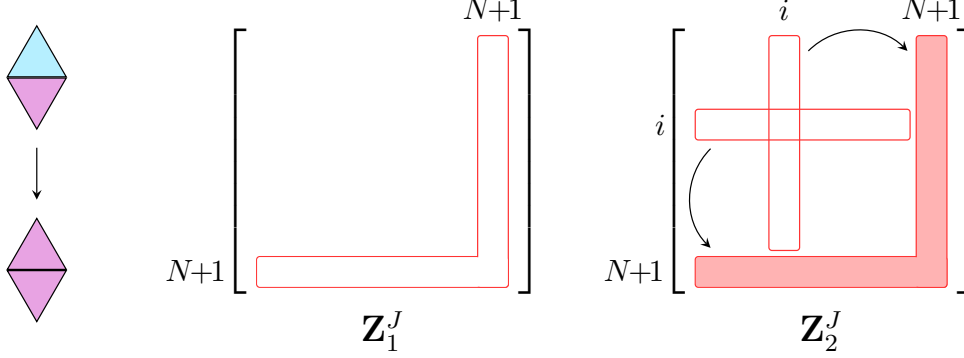
The addition of PEC on only one cell of a function shorts the magnetic currents, leaving the electric ones unchanged due to the dielectric cell left. The rows and columns related to magnetic functions are thus removed from both matrices.



Addition of PEC on a PEC/dielectric function

The last possibility is the addition of PEC on dielectric for a function that is already covered with a conductor in the other cell. Magnetic currents are not present, so no modification is needed for them. Electric currents, instead, are made independent

and the same aforementioned procedure is employed to create a new independent equation from the rows and columns of the modified functions.



Junctions have not been treated due to the complexity involved. This problem is easily overcome by excluding these parts from the optimization process, considering them as fixed features in the structure, which is often the case, for example in feed lines.

5.3 Fitness function

The fitness function is at the core of the optimization process. Its definition influences the convergence of the algorithm to a suitable solution. Care must be exercised in order to take into account the required performances, without slowing the computation too much. In the previous work [14] the focus was on the multi-band behaviour of a compact reconfigurable antenna. For this reason, the design was optimized with respect to the *return loss* at multiple frequency points, with a fitness value equal to the highest RL (worst performance) over all the bandwidth.

Here, instead, the aim is to design directive antennas able to concentrate the radiated energy in a narrow beam. The fitness function must therefore be able to quantify this performance effectively. The choice has been to sample the far field radiation at different equispaced points in spherical coordinates around the z -axis (broadside direction) as in Fig. 5.6. The total radiated power is then obtained by integrating numerically these values:

$$P_{\text{rad}}^{\text{fit}} = \int_0^{2\pi} \int_0^{\theta_1} \frac{|\mathbf{E}^{\text{far}}(\theta, \phi)|^2}{2\eta} \sin \theta \, d\theta d\phi \quad (5.4)$$

$$\approx \frac{1}{2\eta} \sum_{i=1}^N |\mathbf{E}^{\text{far}}(\theta_i, \phi_i)|^2 \sin \theta_i \, \Delta\theta \Delta\phi \quad (5.5)$$

where $\Delta\theta$ and $\Delta\phi$ are the discretization steps.

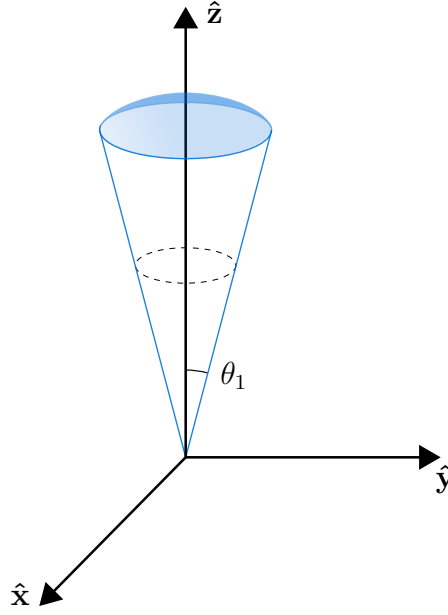


Figure 5.6: Integration region for beam efficiency calculation (broadside direction)

The evaluation of the input matching is still important, since the far field is computed by considering an input voltage of 1V, regardless of the input impedance. This means that the input power is different for each individual:

$$P_{\text{in}} = \frac{1}{2} \text{Re} \left\{ \frac{|V_{\text{in}}|^2}{Z_{\text{ant}}} \right\} = \frac{1}{2} 1V^2 \text{Re} \left\{ \frac{1}{Z_{\text{ant}}} \right\} = \frac{1}{2} 1V^2 \text{Re} \{ Y_{\text{ant}} \}$$

By normalizing the radiated power with respect to the input power, neglecting ohmic losses, the beam efficiency is obtained (Eq. (2.82)).

To take into account the power reflected back to the generator, we should also consider the fraction of input power with respect to the available power of the generator. Thus, a fitness function that takes into account both the beam efficiency and the input matching can be constructed by multiplying these two factors:

$$\text{fitness} = \left(\frac{P_{\text{in}}}{P_{\text{av}}} \right) \cdot \left(\frac{P_{\text{rad}}^{\text{fit}}}{P_{\text{in}}} \right) = (1 - |\Gamma_{\text{in}}|^2) \cdot \text{BE} \quad (5.6)$$

where the input reflection coefficient is calculated from Eq. (2.69), recalled here:

$$\Gamma_{\text{in}} = \frac{Z_{\text{ant}} - Z_0}{Z_{\text{ant}} + Z_0} = \frac{Z_{\text{ant}} - 50 \Omega}{Z_{\text{ant}} + 50 \Omega}$$

Due to the complexity of the optimization strategy, the algorithm could converge

to a solution which has an extremely good directivity, but poor matching properties, as emerged from preliminar tests. This would be undesirable in the validation phase, when the introduced losses can detriment the performances, and the solution would be rendered useless.

To avoid this behaviour, we can assign different exponents to the two factors in order to weight them differently:

$$\text{fitness} = (1 - |\Gamma_{\text{in}}|^2)^\alpha \cdot \text{BE}^\beta \quad (5.7)$$

Since both of them lie in the range $[0,1]$, an exponent > 1 will decrease the relative weight, while if it is between 0 and 1 the weight is increased. In the trial of the optimizer, it has been found that the beam factor usually leads the optimizer to premature convergence. For this reason, a value of α between 3 and 5 is chosen, while β is kept between 0.3 and 0.6.

5.4 Computational cost reduction techniques

A series of techniques have been devised in order to reduce the computational bargain posed by large problems. Geometric symmetry and inherent parallelism of the optimizer are discussed next.

5.4.1 Geometric symmetry

A quite common solution for the reduction of problem size is that of considering an infinite ground plane, instead of a finite one, with PEC boundary conditions. Its presence is taken into account by modifying the Green's function. Considering a current radiating in presence of the ground plane, from image theory [3], we can conclude that an image source can be placed below the ground plane with the orientation given in Fig. 5.7. The field in the upper space is the superposition of those radiated in free space by the original and image sources.

A further simplification can be achieved by exploiting symmetries in the geometry: if we allow a reduction of the solution space by considering only those structures with a defined symmetry plane, we only need to simulate half of the problem, relying on symmetry for the reconstruction of the complete one. This assumption does not affect the algorithm effectiveness, since most actual design require symmetric radiation patterns.

Currents cannot flow perpendicularly to the symmetry plane, otherwise they would violate physical symmetry. For the same reason, current must be mirrored across the plane. This produces a purely normal electric field on it, which is equivalent to a PMC boundary condition as shown in Fig. 5.8.

The electromagnetic problem can be formulated equivalently considering half of the structure with a symmetry plane over which PMC boundary conditions are

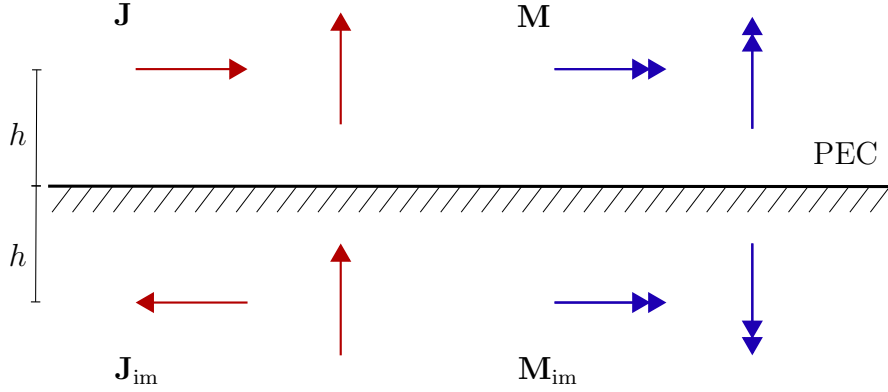


Figure 5.7: Image currents orientation for a PEC ground plane

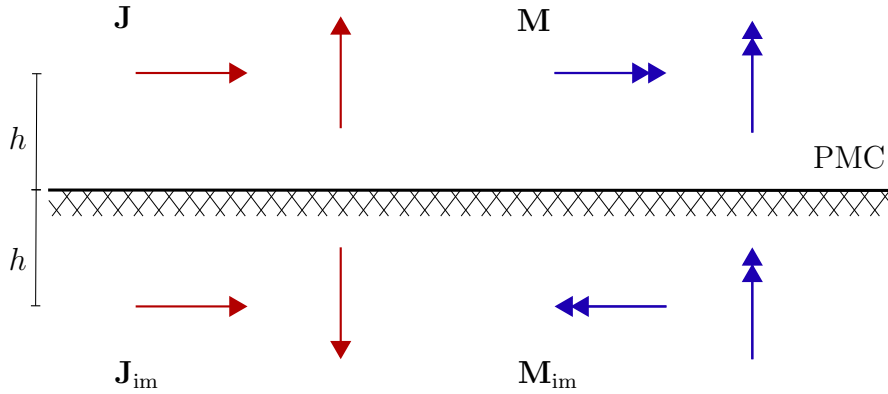


Figure 5.8: Image currents orientation for a PMC plane

enforced, as schematized in Fig. 5.9.

Regarding the pre-process phase, this modification is easily implemented: since no current can flow perpendicular to the symmetry plane at the intersection, there's no need to place basis functions there, much like for a real boundary. This means that the geometry can be drawn for only half of the structure, without further modification needed. Also the feed need to be symmetric. The input impedance is then halved with respect to the simulated one:

$$Z_{\text{ant}} = \frac{1}{2} Z^{\text{sym}} \quad (5.8)$$

since two identical half-structures are placed in parallel from the input standpoint.

It is important to note that, contrary to the infinite ground plane assumption, this technique relies on true geometric symmetry. Therefore, it does not introduce any approximation in the solution.

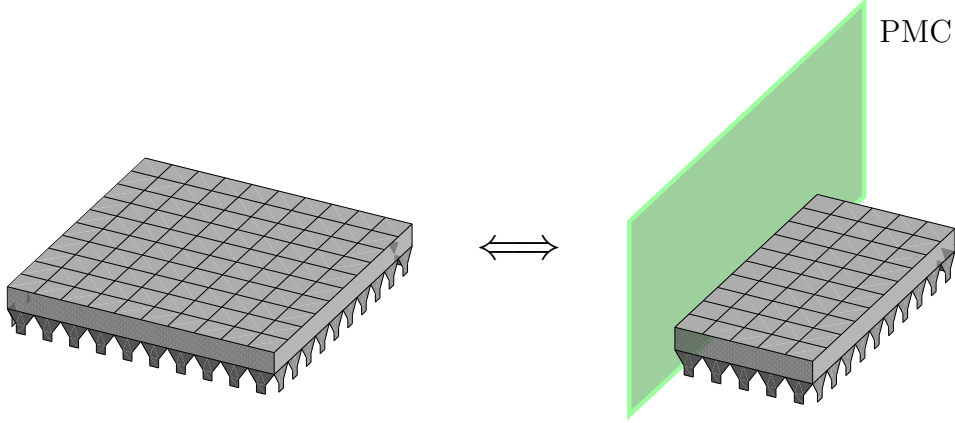


Figure 5.9: Geometric symmetry: full structure (left) and equivalent symmetric problem with PMC boundary condition at $x = 0$ (right)

The EM solver will take into account image sources by modifying the Green's function. Limiting the analysis to electric currents, if we consider a PMC plane place at $x = 0$, the radiation operators become:

$$\mathbf{E}(\mathbf{r}) = -\eta \mathcal{L}^{\text{sym}}[\mathbf{J}](\mathbf{r}) \quad (5.9)$$

$$\mathbf{H}(\mathbf{r}) = -\mathcal{K}^{\text{sym}}[\mathbf{J}](\mathbf{r}) \quad (5.10)$$

where

$$\begin{aligned} \mathcal{L}^{\text{sym}}[\mathbf{J}](\mathbf{r}) &= \mathcal{L}[\mathbf{J}](\mathbf{r}) + \mathcal{L}[\mathbf{J}_{\text{im}}](\mathbf{r}) = \\ &= jk \int_{\mathcal{D}} G(\mathbf{r}, \mathbf{r}') \mathbf{J}(\mathbf{r}') d\mathcal{D}' - \frac{1}{jk} \nabla \int_{\mathcal{D}} G(\mathbf{r}, \mathbf{r}') \nabla' \cdot \mathbf{J}(\mathbf{r}') d\mathcal{D}' \\ &+ jk \int_{\mathcal{D}_{\text{im}}} G(\mathbf{r}, \mathbf{r}'_{\text{im}}) \mathbf{J}_{\text{im}}(\mathbf{r}'_{\text{im}}) d\mathcal{D}' - \frac{1}{jk} \nabla \int_{\mathcal{D}_{\text{im}}} G(\mathbf{r}, \mathbf{r}'_{\text{im}}) \nabla' \cdot \mathbf{J}_{\text{im}}(\mathbf{r}'_{\text{im}}) d\mathcal{D}' \end{aligned} \quad (5.11)$$

$$\begin{aligned} \mathcal{K}^{\text{sym}}[\mathbf{J}](\mathbf{r}) &= \mathcal{K}[\mathbf{J}](\mathbf{r}) + \mathcal{K}[\mathbf{J}_{\text{im}}](\mathbf{r}) = \\ &= \int_{\mathcal{D}} \mathbf{J}(\mathbf{r}') \times \nabla G(\mathbf{r}, \mathbf{r}') d\mathcal{D}' + \int_{\mathcal{D}_{\text{im}}} \mathbf{J}_{\text{im}}(\mathbf{r}'_{\text{im}}) \times \nabla G(\mathbf{r}, \mathbf{r}'_{\text{im}}) d\mathcal{D}' \end{aligned} \quad (5.12)$$

The image quantities are related to the original ones by:

$$\begin{aligned}\mathbf{r}_{\text{im}} &= -r_x \hat{\mathbf{x}} + r_y \hat{\mathbf{y}} + r_z \hat{\mathbf{z}} \\ \mathbf{J}_{\text{im}}(\mathbf{r}_{\text{im}}) &= -J_x(\mathbf{r}) \hat{\mathbf{x}} + J_y(\mathbf{r}) \hat{\mathbf{y}} + J_z(\mathbf{r}) \hat{\mathbf{z}}\end{aligned}$$

A depiction of the radiation of original and image sources for a symmetric structure is shown in Fig. 5.10.

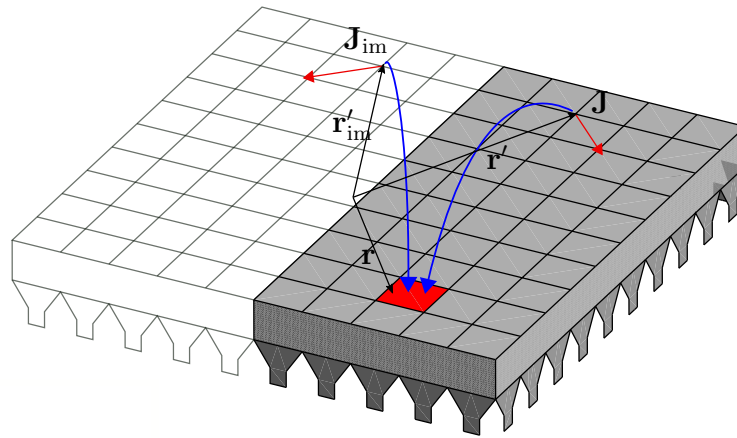


Figure 5.10: Radiation of original and image currents to a point \mathbf{r} for calculation of the interaction matrix

5.4.2 Code parallelization

The most computation intensive step is the fitness calculation for each individual, which requires the solution of a rather large linear system, depending on the mesh fineness. A significant reduction of simulation time can be obtained by exploiting the intrinsic parallelism of the genetic algorithm. In fact, each individual can be evaluated independently of others, allowing to run multiple instances at the same time on different threads of a multicore structure. To this purpose, the code has been modified making use of the `parfor` command provided by Matlab *Parallel Computing Toolbox*, which runs a `for` loop in a parallel fashion.

With the computation resources provided by HPC@POLITO, the code has been deployed to a cluster node composed of 16 cores, with a sensible reduction in the overall simulation time.

Chapter 6

Results

This chapter presents the results obtained with the proposed optimization procedure. The code has been applied to large planar antennas with different geometries and feed mechanisms. The optimization parameters, as well as resulting structure are described for each case.

6.1 Optimization of multiband antenna

Before attempting to optimize large structures, the code has been applied to the design presented in [14]. Here, a compact multiband reconfigurable antenna was considered. It is composed of an upper patch of size $0.17\lambda \times 0.17\lambda$, connected to ground through 40 straps around the border, each representing a switch. The patch is excited by means of an L-feed which is also optimizable.

The employed approach is to optimize both the patch and the switches together: first, the matrix is solved and a multiport S -matrix is obtained, then an exhaustive search among all switch configurations is performed to recover the best switch pattern at each considered frequency in terms of *return loss*. The fitness is then equal to the worst performance over the bandwidth:

$$\text{fitness}_{\text{RL}} = \max_f \{ \min_i \{ 20 \log_{10} |\Gamma_{\text{in}}(f, \text{sw}_i)| \} \} \quad (6.1)$$

Switches are modeled as ideal open and closed circuit, and they can be removed by the optimization of metal straps to which they are attached. It is clear that a large number of switches will likely result in better performances. However, since each switch must be driven, the complexity of the network (not considered here) grows accordingly, balancing the performances. For this reason, the total number of switches has been considered as a penalty in the fitness evaluation, with a linear

combination of factors:

$$\text{fitness} = \alpha \text{fitness}_{\text{RL}} + \beta \frac{1}{N_{\text{sw}}} \quad (6.2)$$

In order to initialize the population efficiently, a series of consideration have been made. First, a design with plenty of metal will result in a more robust structure once it is realized; this is especially important if, as in this case, the inside is filled with air and no dielectric supports the patch. For this reason, the metallic surfaces of individuals have been initialized with an higher probability of being present (around 70% – 80%).

Following the same reasoning, if a large number of switches is present from the beginning, it will slow down the optimization process. In this case the choice is to place switches with an initial probability of 20%.

All the important parameters of the genetic algorithm are summarized in Tab. 6.1.

Parameter	Value
Generations	300
Population size	400
Chromosome length	156
Fitness	$\text{RL} + N_{\text{sw}}$
Crossover	2-points
Selection	rank-based
Mutation rate	0.3%
Spontaneous	2%
Elite	1%

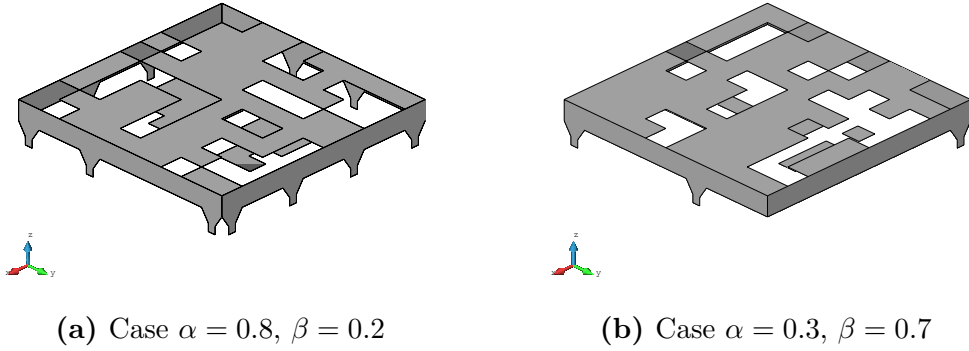
Table 6.1: Summary of GA parameters

Each structure has been simulated at 10 linearly spaced frequencies between 1.7 GHz and 2.7 GHz. Two different runs of the algorithm have been made, with different weights for the cost function. In the first case, the focus was on the input matching, while in the second one a lower number of switches has been preferred by increasing the relative weight. Results are summarized in Tab. 6.2, while optimized structures are shown in Fig. 6.1a and 6.1b.

Plots of the input matching for the two cases are reported in Fig. 6.2. It is clear that an higher number of switches results in much better performances, at the expense of a complicated driving network.

It can be interesting to look at the different switch configurations: in Fig. 6.3a it is clear that most of the switches are needed to obtained the prescribed behaviour over all the bandwidth. In particular, only switch 11 is always open, meaning that

	$\alpha = 0.8$ $\beta = 0.2$	$\alpha = 0.3$ $\beta = 0.7$
$S_{11\max}$	-10.08 dB	-15.85 dB
$S_{11\min}$	-30.09 dB	-43.90 dB
N° switch	14	4
Opt. time	12h34m	15h12m

Table 6.2: Optimization results**Figure 6.1:** Resulting structures for the two cases

it can be removed without modifying the performances. In Fig. 6.3b, as expected, a lower number of switches results in a simpler configuration.

It is useful to compare the simulation time for the two cases: as expected, when the input matching is favored the number of switches increases quickly and the simulation time for each generation increases exponentially (Fig. 6.4a) due to the time required to explore all the $2^{N_{\text{sw}}}$ possible configurations. In the second case, instead, the number of switches does not increase significantly from one generation to the next, yielding an almost constant simulation time per generation, as shown in Fig. 6.4b.

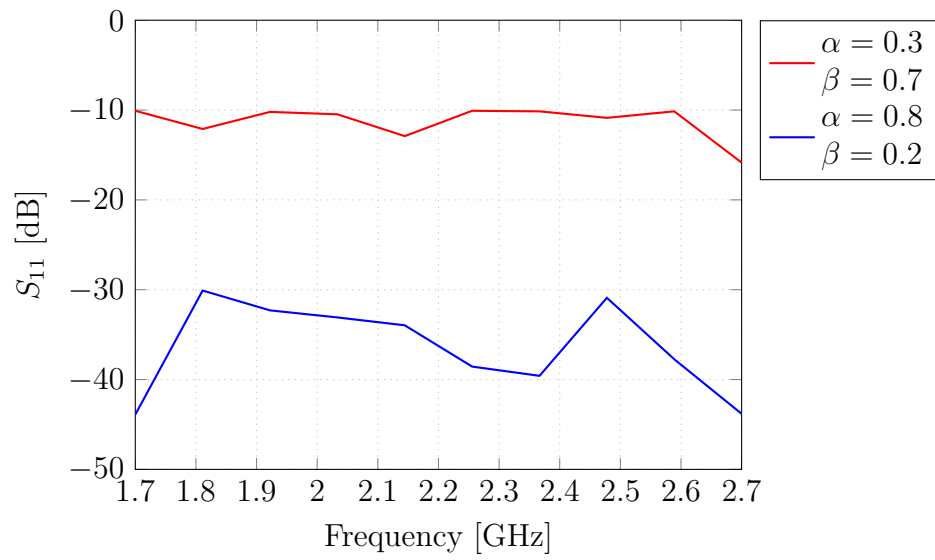
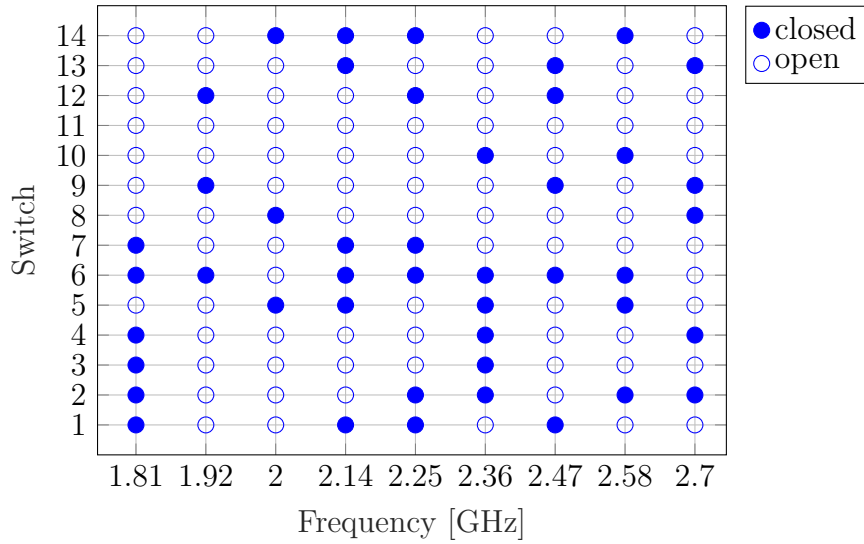
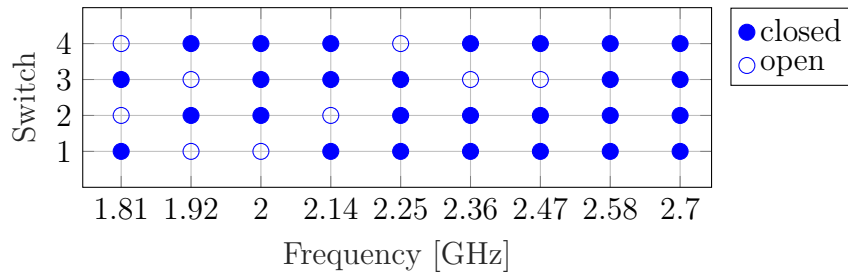
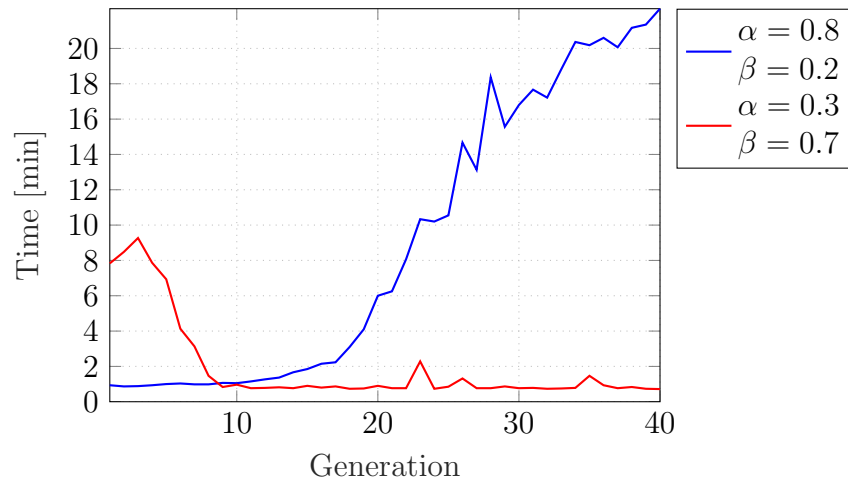
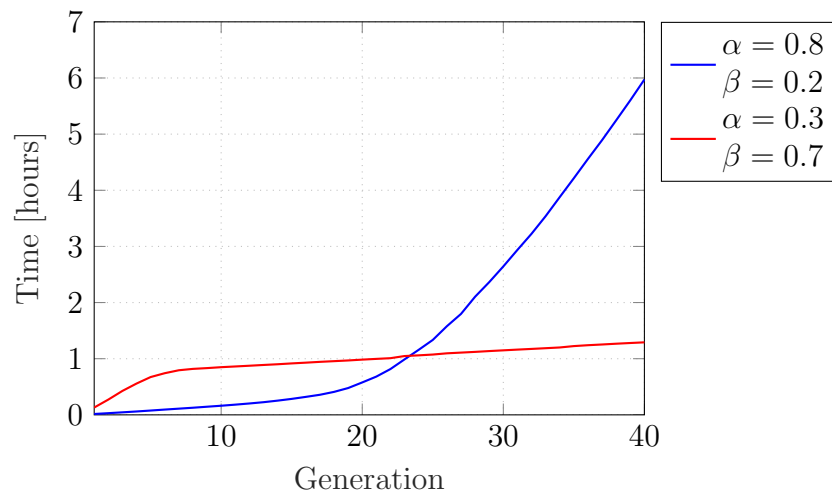


Figure 6.2: S_{11} of the two optimized structures

(a) Case $\alpha = 0.8, \beta = 0.2$ (b) Case $\alpha = 0.3, \beta = 0.7$ **Figure 6.3:** Switch patterns for the two cases



(a) Simulation time for each generation



(b) Total simulation time

Figure 6.4: Simulation time comparison (only the first 40 generations are shown for clarity)

6.2 Pin fed planar antenna

In order to obtain a low-profile directive antenna, a planar geometry has been considered. It consists of an upper patch of dimensions $2\lambda \times 2\lambda$ suspended above a ground plane. The antenna is fed through a small pin placed at the center of the patch (Fig. 6.14a). Since the simulator can only deal with surfaces, the pin has been modeled as a thin strip, with a width much shorter than a wavelength, respecting the symmetry imposed by the model (fig. 6.5).

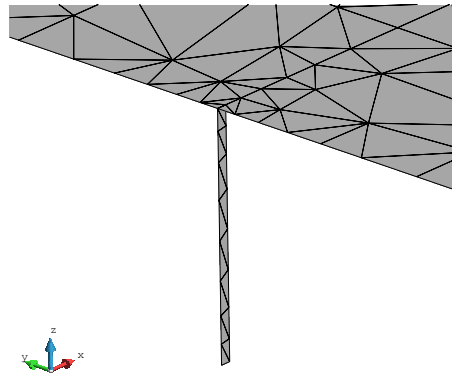


Figure 6.5: Particular of the pin feed modeling with assigned mesh

6.2.1 Infinite ground plane

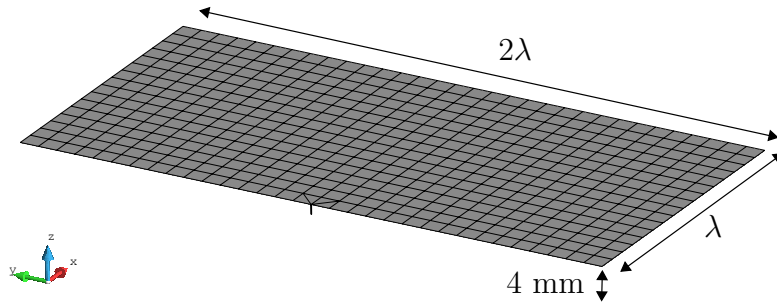
In the first iteration, the structure has been simulated above an infinite ground plane at $z = 0$ and with a symmetry plane at $x = 0$. This allowed to benchmark the simulation time and the feasibility of the expected performances. The optimizable portions have been chosen to cover all the upper patch, with square sectors of dimensions $\lambda/16 \times \lambda/16$. A guard area has been left around the feed junction to ensure a correct excitation, as can be seen in Fig. 6.14b. The whole structure has been meshed adaptively with a finer resolution ($\approx \lambda/30$) near the feed and a coarser one ($\approx \lambda/16$) far away from it (Fig. 6.6c).

The used GA parameters are listed in table 6.3.

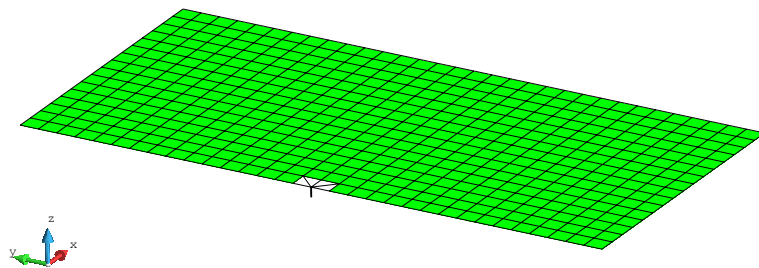
The resulting geometry is shown in Fig. 6.7.

6.2.2 Finite ground plane

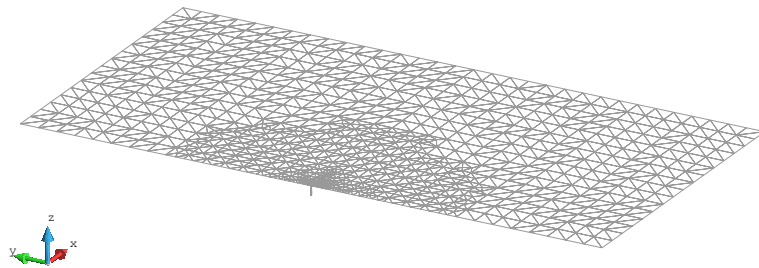
The same structure has been optimized embedding the finite ground plane in the simulation. The ground plane is essentially a rectangular conductor, without sophisticated features and as such it has been meshed with a coarser resolution with



(a) Half structure



(b) Optimization mask (green)



(c) Mesh

Figure 6.6: Pin fed planar antenna

respect to the upper patch. The geometry is shown in Fig. 6.8a. The optimization mask and mesh for the upper patch are the same of Fig. 6.6, while a cut of the ground plane is shown in Fig. 6.8b to highlight the mesh.

A comparison of the performances with infinite and finite ground plane are summarized in Tab. 6.4, while far field patterns are shown in Fig. 6.9 for the two cases.

Parameter	Value
Generations	300
Population size	500
Chromosome length	510
Fitness	RL+FF
Weights	$\alpha = 4, \beta = 0.6$
Crossover	2-points
Selection	roulette-wheel
Mutation rate	0.3%
Spontaneous	2%
Elite	1%

Table 6.3: Summary of GA parameters for pin fed structure

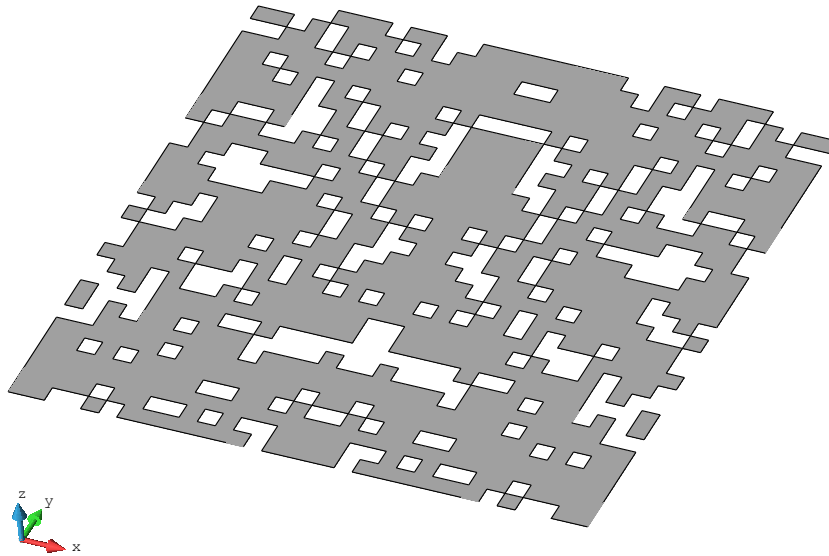
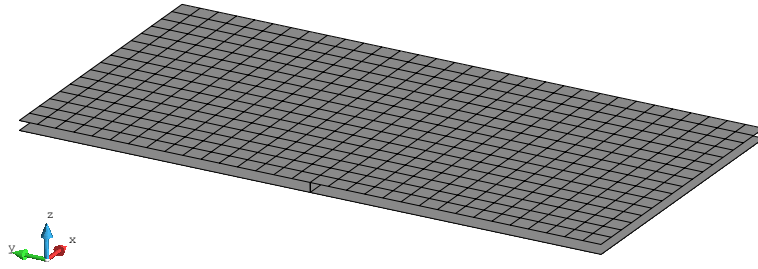


Figure 6.7: Optimized design with pin feed and infinite ground plane

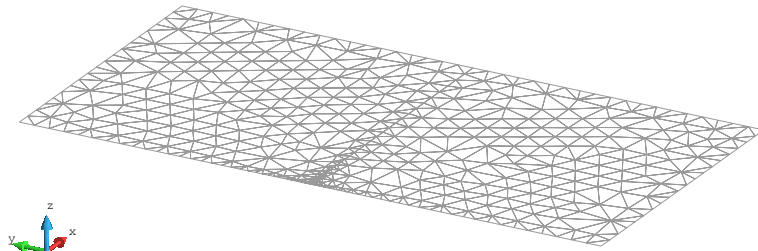
6.2.3 Coaxial feed

To model the source in a realistic way, the structure in Fig. 6.7 has been modified with a coaxial feed. This resulted in the structure of Fig. 6.10, where a piece of coaxial with a length of $\lambda/10$ has been placed below the ground plane, with the inner conductor extending to contact the upper patch. A waveguide port has been placed on the cable cross section at a distance of $\lambda/10$ from the ground plane.

A simulation has been run in CST, with a frequency span from 2.2 GHz to



(a) Structure



(b) Cut of the ground plane mesh

Figure 6.8: Pin fed planar antenna with finite ground plane

	S_{11} [dB]	D_{\max} [dBi]	HPBW	η_{ap}
Inf. ground	-8.36	17.73	23.6°	1.18
Finite ground	-6.16	16.33	24.48°	0.85

Table 6.4: Comparison of pin fed structure in presence of infinite and finite ground plane

2.8 GHz. It is clear from Fig. 6.11 that the resonance frequency shifts below the one optimized with the pin feed, which oversimplifies the behaviour. Nonetheless, although being very directive, the structure maintains a sufficient matching of at least -6 dB over a frequency range from 2.25 GHz to 2.45 GHz.

The directivity of the optimized antenna is shown in Fig. 6.12. In this case, the backlobe radiation is significant, due to a more realistic feed modeling.

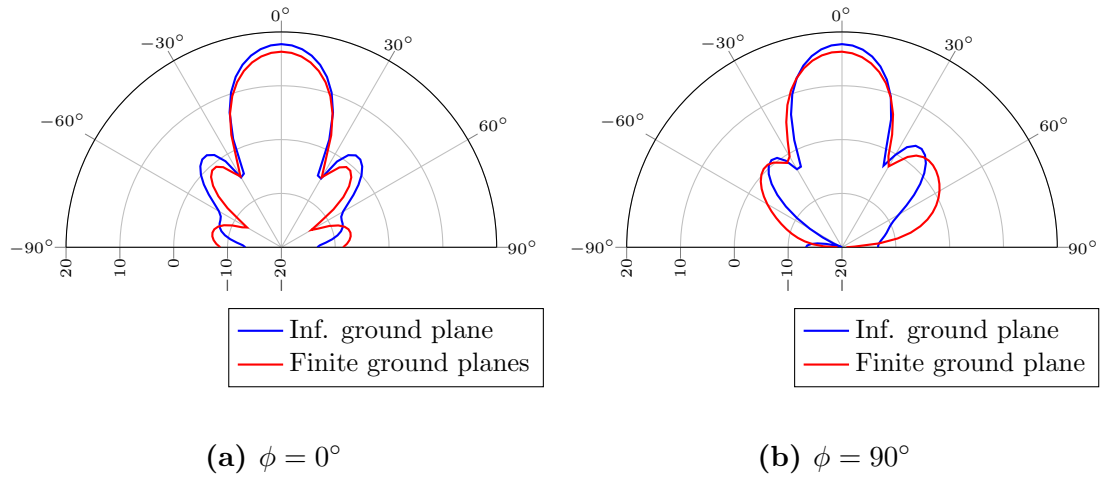


Figure 6.9: Far field directivity [dBi] of pin feed design with infinite and finite ground plane

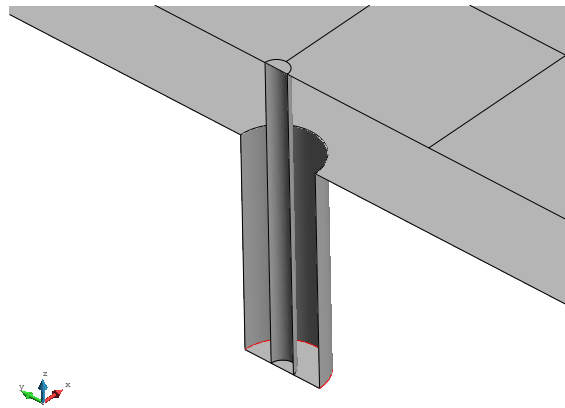


Figure 6.10: Coaxial feed model with lumped source excitation (red)

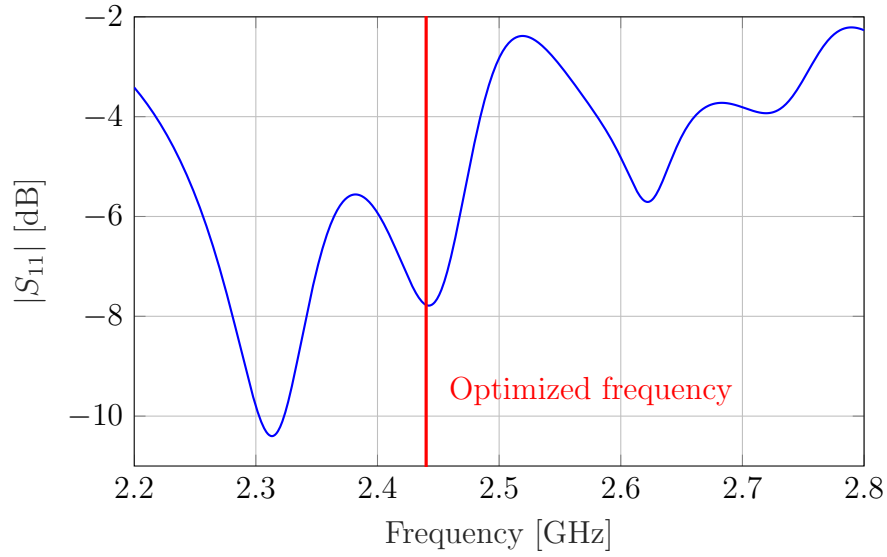


Figure 6.11: $|S_{11}|$ of the coaxial fed structure

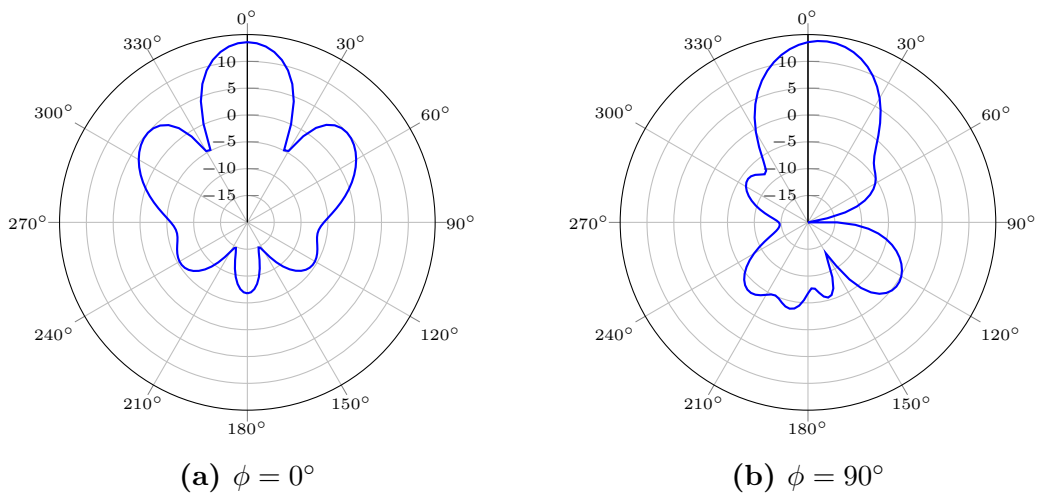


Figure 6.12: Far field directivity [dBi] of coaxial fed structure

6.3 Slot coupled microstrip planar antenna

Performances obtained with the pin fed patch were not satisfactory in terms of bandwidth. This is probably due to the pin itself, which has a narrow frequency response. Therefore, a slightly different feed mechanism has been considered: it consists of a rectangular aperture on the ground plane, fed by a microstrip transmission line placed on a substrate below the ground plane. An advantage of this feeding, known as *aperture coupling* [13], is that the feed network is isolated from the radiating element by the ground plane, which prevents spurious radiation.

A cross section of the microstrip line is shown in Fig. 6.13a, while the slot dimensions are reported in Fig. 6.13b. To improve coupling, a stub of length $\lambda/4$ has been placed on the microstrip line beyond the slot.

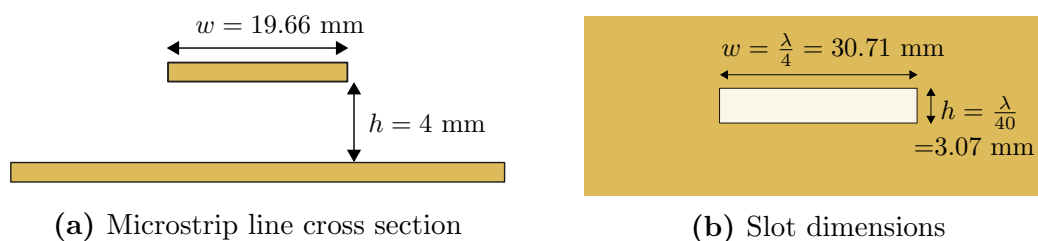


Figure 6.13: Feeding characteristics

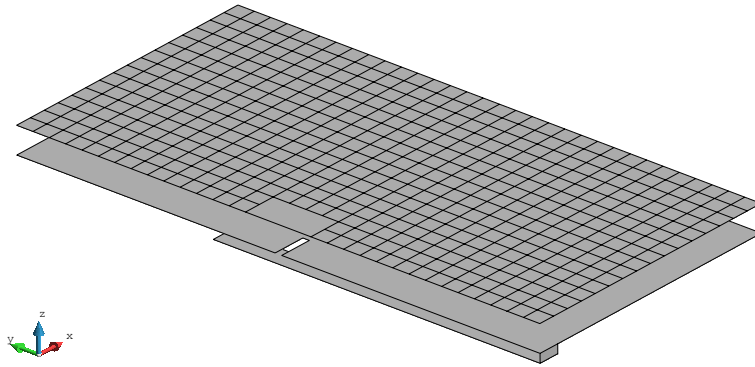
The upper patch has been subdivided in 504 optimizable sectors, each with dimensions $\lambda/16 \times \lambda/16$, with a guard area above the slot in order to ensure a correct coupling between the microstrip feed and the upper patch (Fig. 6.14). The meshing of the structure is detailed in Sec. 6.4.2, where an in-depth analysis is carried out on the mesh accuracy.

GA parameters used are summarized in Tab. 6.5. With respect to previous runs, the size of the population has been slightly decreased and the crossover is done based on ranking to prevent a premature convergence of the algorithm. The optimization took about 15 hours, after which the resulting geometry of Fig. 6.15 was obtained.

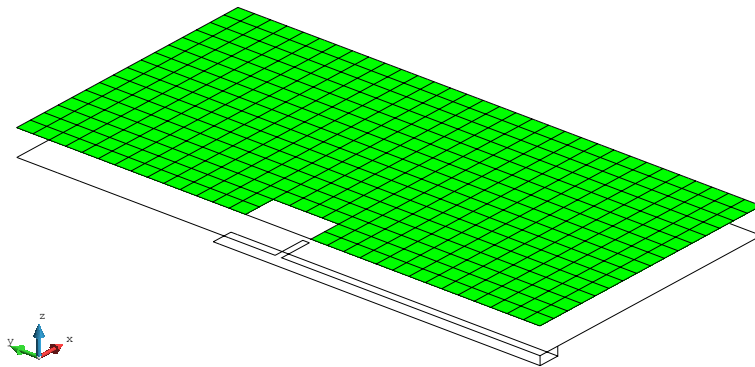
A frequency sweep has been simulated to check the bandwidth of the optimized structure. As can be seen in Fig. 6.16, the resonance has shifted slightly to a higher frequency of 2.51 GHz. The reflection coefficient is coherent with the optimized values.

The resulting radiation pattern are shown in Fig. 6.17 for the optimized frequency and for the resonance one.

A summary of the performances is presented in Tab. 6.6.



(a) Half structure



(b) Optimization mask (green)

Figure 6.14: Slot coupled planar antenna

Parameter	Value
Generations	500
Population size	400
Chromosome length	504
Fitness	RL+FF
Weights	$\alpha = 3, \beta = 0.8$
Crossover	2-points
Selection	rank-based
Mutation rate	0.3%
Spontaneous	2%
Elite	1%

Table 6.5: Summary of GA parameters for slot coupled structure

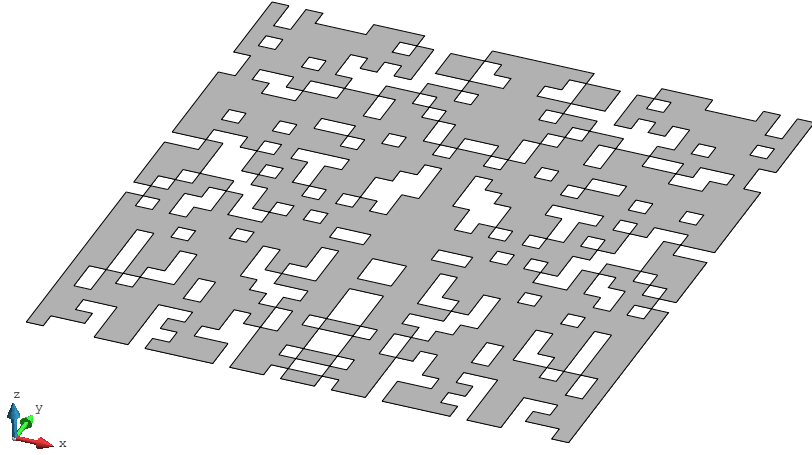


Figure 6.15: Optimized design for slot coupled structure (ground plane not shown for clarity)

	S_{11} [dB]	D_{\max} [dBi]	HPBW	η_{ap}
Slot coupled	-6.8	14.15	22.44°	0.51

Table 6.6: Comparison of pin fed structure in presence of infinite and finite ground plane

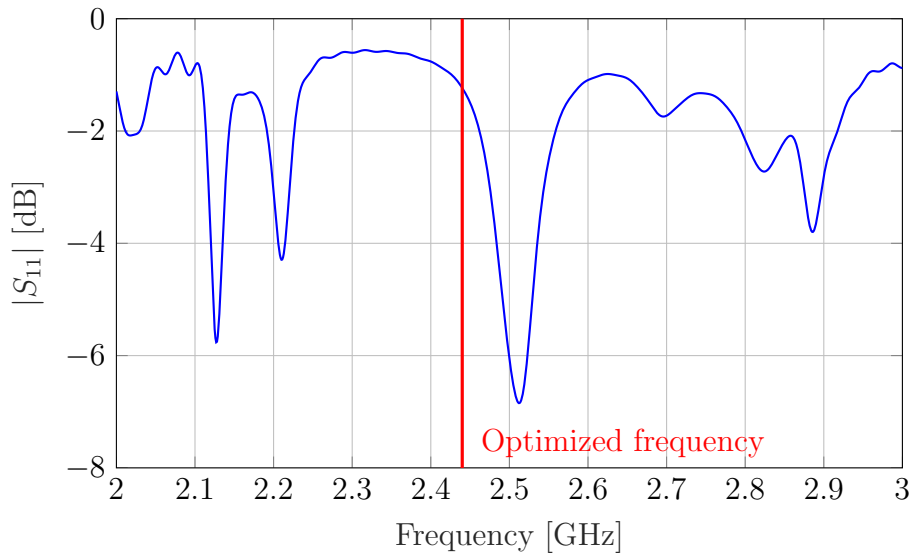


Figure 6.16: $|S_{11}|$ of the slot coupled structure

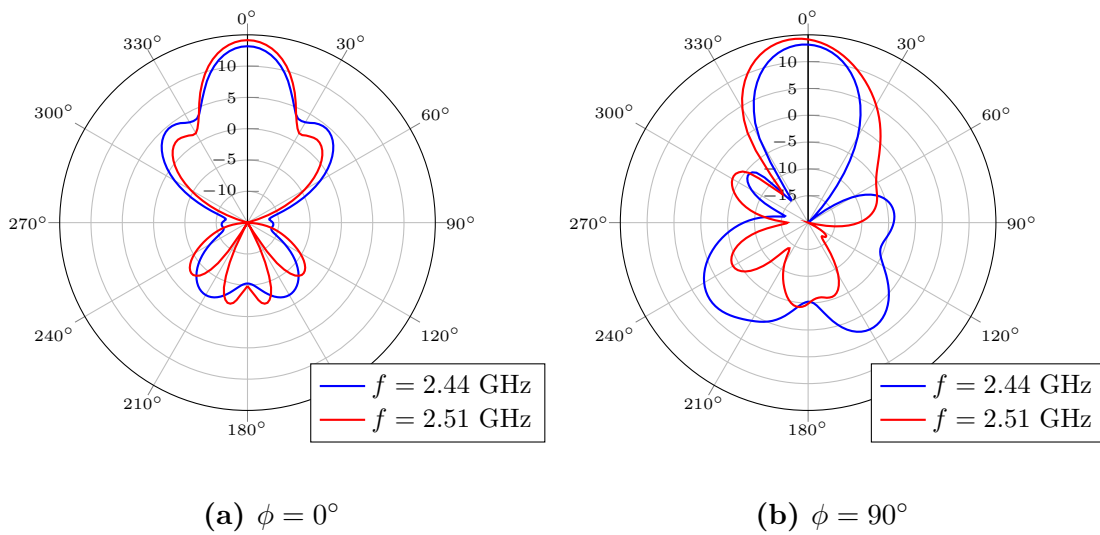


Figure 6.17: Far field directivity [dBi] in the two principal planes, at 2.44 GHz (optimized frequency) and 2.51 GHz (resonance)

6.4 Modeling evaluation

6.4.1 Effect of mesh singularities

During the optimization process it frequently happens that, in the resulting structure, two nearby metal sectors share a common node without touching each other (Fig. 6.18). The employed mesh will therefore be singular, without the ability to represent real situations. This can cause problems in the prototyping phase where, due to fabrication tolerances, regions that are not meant to overlap can slightly touch, allowing current to flow between them. Thus, the optimization mesh can not be considered reliable with respect to the final prototype.

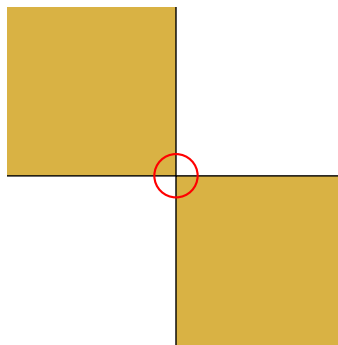


Figure 6.18: Mesh singularity

For this reason, in the postprocessing phase all singular points are removed by trimming the edges near corners (Fig. 6.19). The geometry can be then meshed again and simulated with a commercial EM software. Results did not show significant changes in the radiation pattern, as can be seen in Fig. 6.20 for the two principal planes, with slight differences probably due to the different meshes employed.

This process has been automated by creating a custom geometry that can be subsequently subtracted from the original one by a boolean operator on surfaces.

Microstrip source definition

The definition of the source excitation for microstrip lines is particularly challenging, since the MoM can only deal with lumped edge sources. Different approximations have been tested, placing a shorting wall at the beginning of the microstrip. The source has been placed in three different positions, as shown in Fig. 6.21. No significant changes in the obtained input impedance have been noticed between them. For simplicity, all subsequent models have been simulated with the configuration of Fig. 6.21c.

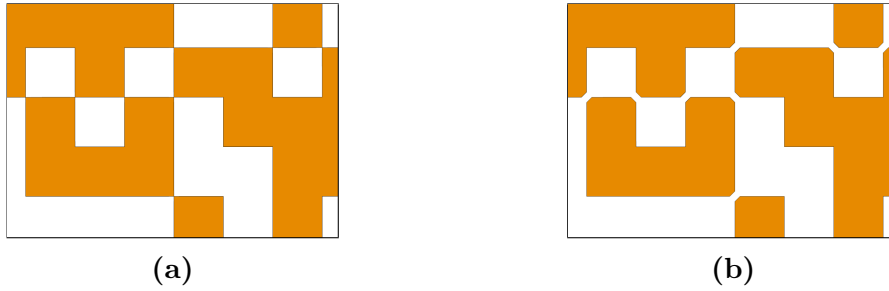


Figure 6.19: Example of optimized structure features: before (a) and after (b) the trimming process to remove mesh singularities

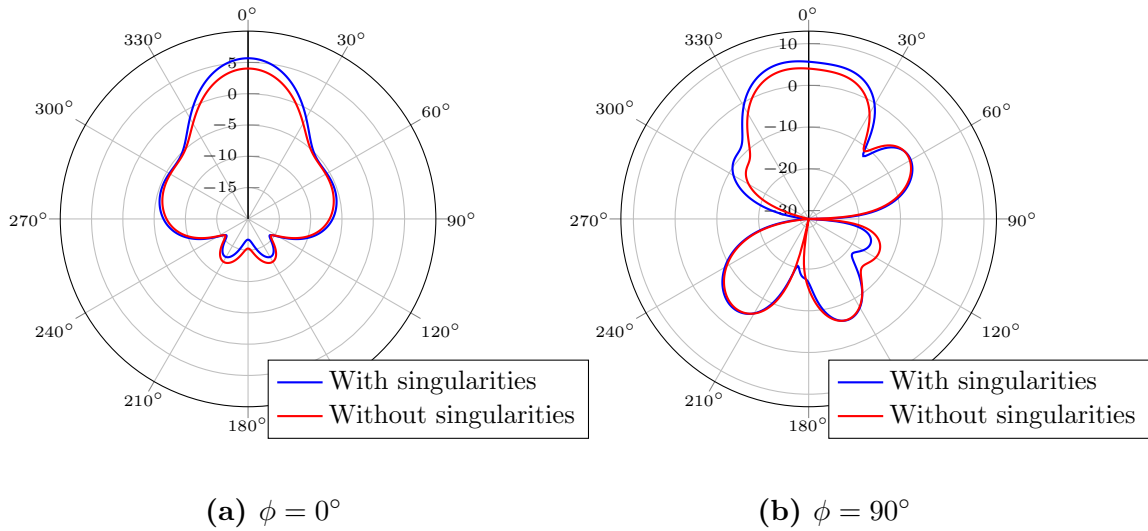


Figure 6.20: Far field directivity [dBi] in the two principal planes, before and after the removal of singularities

6.4.2 Mesh size

Large discrepancies have been found in the calculation of the input impedance in relation to the mesh size. In particular, for a thin microstrip height of about 1 mm, the resolution must be on the order of $\lambda/240$ to model the feed correctly. This is due to the inherent limit of the mesh resolution when geometrical features are much smaller than the wavelength. Moreover, at the feed edge, the mesh must be fine enough to describe the current distribution along the width of the microstrip.

For this reason, a parametric analysis has been carried out. In FEKO, a simple slot coupled rectangular patch of dimensions $\lambda/2 \times \lambda/2$ has been simulated above a

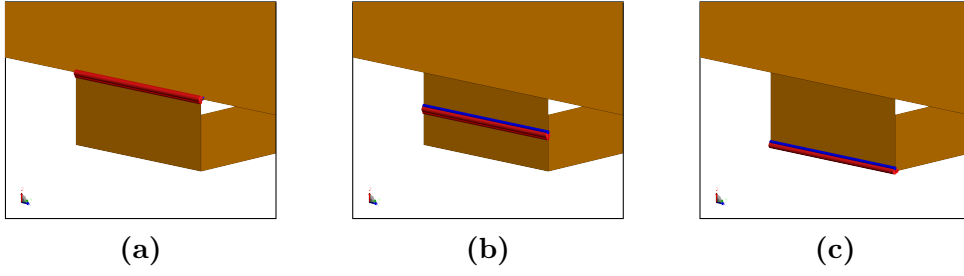


Figure 6.21: Different positions for the lumped edge source on the microstrip line: at the junction with the ground plane (a), in the middle (b) and at the height of the microstrip (c)

ground plane, for different mesh sizes. Since the modeled structure is well known for

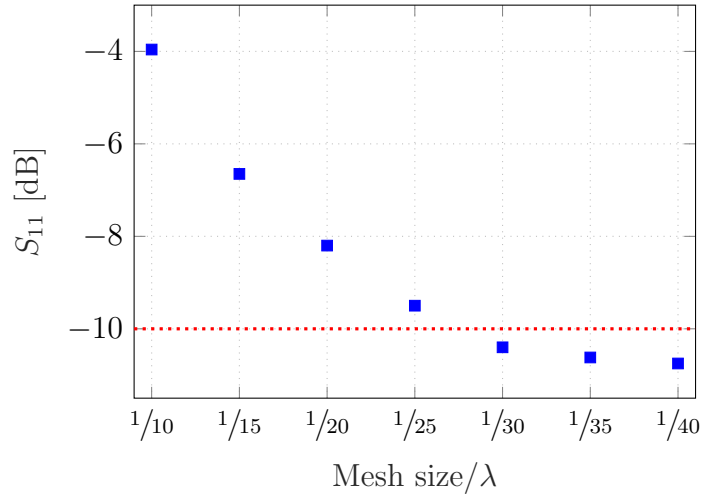


Figure 6.22: S_{11} as a function of mesh size (normalized to the wavelength)

its good matching properties, a computed S_{11} of around -10 dB has been considered reliable. As indicated by Fig. 6.22, a mesh with a dimension of $\lambda/30$ has been deemed suitable for the optimization, considering the trade-off with computation time.

Moreover, it has been found that the upper patch mesh is crucial in the simulation phase. This can be explained considering that, due to the optimization process, different metal parts are removed randomly. Without an a priori knowledge of the final geometry, it is almost impossible to forecast where the electromagnetic field will have the fastest variations. This means that a conservative resolution must be chosen onto and near optimizable surfaces.

On the contrary, the mesh on ground plane can be relaxed, since the geometry is regular and fixed. To sum up, the upper patch and the microstrip line have been meshed with a size of $\lambda/30$, while for the ground plane a dimension of $\lambda/10$ has been chosen (with a refinement below the microstrip) as shown in Fig. 6.23.

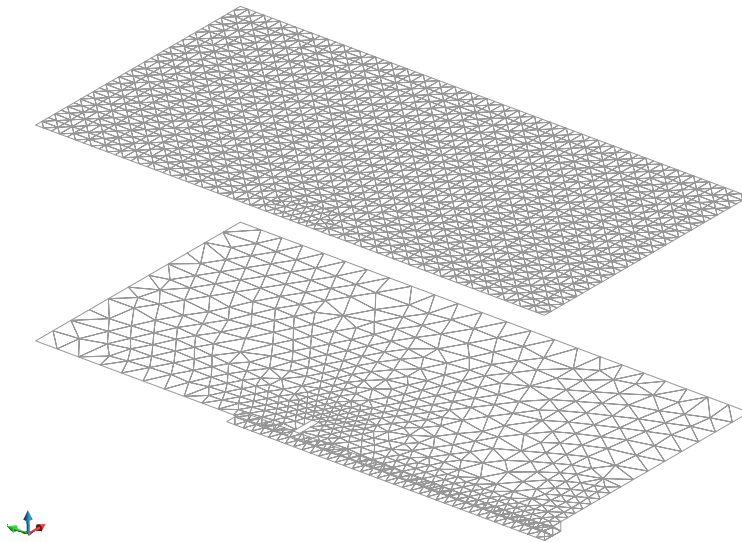


Figure 6.23: Exploded view of the upper patch and ground plane mesh

6.5 Prototyping

After a thorough validation of the design optimized in Sec. 6.3, the next step involved the prototyping of the structure. Due to the complex geometry, a series of techniques have been used to reproduce a faithful real model.

6.5.1 Layout

Since the structure was optimized in air, a need for a dielectric to provide mechanical support to the structure arose. This prompted the choice of ROHACELL 31HF, a foam based material with low dielectric constant and negligible absorption in the high frequency range, so as to approximate as good as possible the electrical properties of air. The final layout is schematized in Fig. 6.24.

Due to the intricate geometry of the upper patch, a mask has been manufactured in resin with a laser 3D printer (Fig. 6.25). This procedure allowed a low cost, fast prototyping with a satisfactory precision.

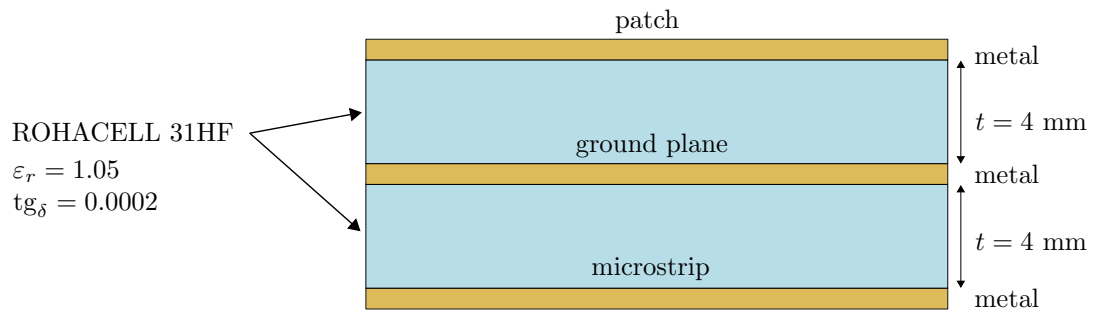


Figure 6.24: Layout of the prototyped structure

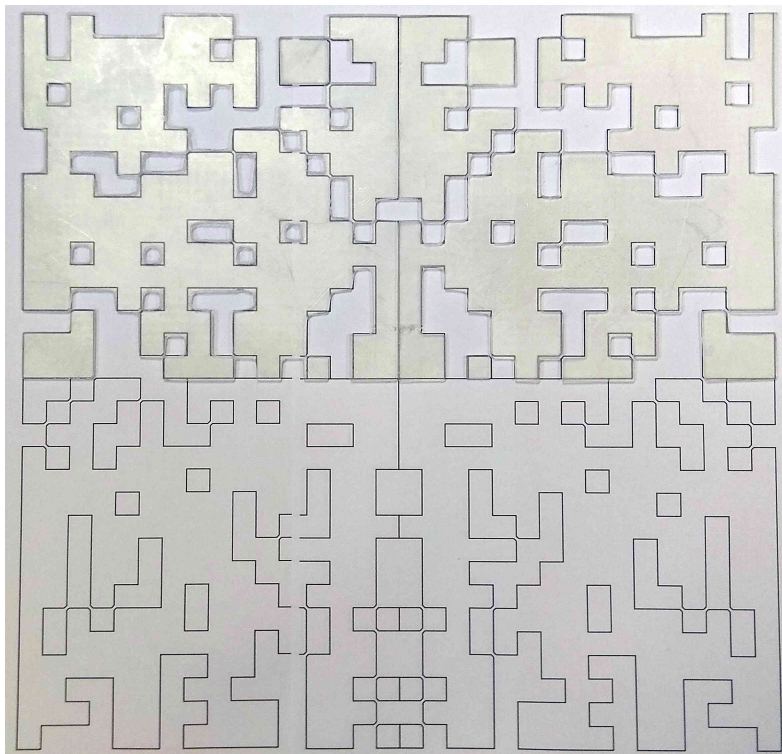


Figure 6.25: Manufactured resin mask placed over the geometry outline

Chapter 7

Conclusions

This work presented a novel approach to the optimization of directive antennas. By virtue of an efficient combination of computational methods and optimization algorithms, the automated design of complex antennas has been demonstrated to be feasible.

The proposed method allows to model large structures with full-wave accuracy, giving results that require only minor modifications in the post-process phase.

Due to the large size of solution space, results are characterized by non-intuitive geometries, which would not be conceivable with analytical tools.

Different starting structures have been tested, for which the resulting optimized design have been validated with the help of commercial softwares. The impact of mesh dimensions have been investigated, finding satisfactory trade-offs between accuracy and solution time.

Future developments can include:

- combination of directive antennas with reconfiguration capability to allow the optimization of beam reconfigurable antennas
- inclusion of bandwidth constraints in the optimization, which requires the computation of one matrix for each considered frequency
- addition of dielectrics in the simulation of large structures, for which a convenient formulation has been developed. However, at the moment, the resulting size of numerical problem limits its application to real cases
- refinements the objective function, taking into account the complexity of the resulting structure and different performances, for example the polarization properties of radiated fields
- improvements in the solution of the linear system resulting from the discretization, through matrix partitioning of portions of the modeled structure which are not modified during optimization

Appendix A

GiD *Problem type*

One of the goals of this work was the creation of a suitable procedure to define an optimizable design, regardless of the employed code. This has been achieved by exploiting the customization offered by the GiD preprocessor. In particular, the software allows to define custom *problem types*, namely a set of arbitrary conditions that can be applied over simulation entities and are then transferred to the corresponding mesh elements.

```
CONDITION: Sector
    CONDTYPE: over surfaces
    CONDMESHTYPE: over body elements
    QUESTION: SectorNumber
    VALUE: 1
END CONDITION

CONDITION: Optimize
    CONDTYPE: over surfaces
    CONDMESHTYPE: over body elements
END CONDITION
```

First of all, the geometry must be drawn with each optimizable sector defined as a different surface, even if it is coplanar with other adjacent ones. Then, to obtain the sector mapping described in Sec. 5.1, a boolean condition, named *optimize*, is applied over all the surfaces that the designer wishes to optimize. The last step requires the numbering of each sector with a progressive index; in a realistic case, the number of sectors could reach the hundreds, so the indexing process has been automated with a customized macro written in Tcl/Tk language.

```
proc ::assign_sector {} {
  set point_ids [list]
  foreach item [GiD_Info conditions Optimize geometry] {
    lappend sector_ids [lindex $item 1]
  }
  set sector_ids [lsort $sector_ids]
  for { set index 0 } { $index < [llength $sector_ids] }
    { incr index } {
    GiD_AssignData condition Sector Surfaces [expr
      $index +1] [lindex $sector_ids $index]
  }
}
```

Having done these steps, the structure can finally be meshed and all required informations are passed to the optimizer code by means of custom generated text files.

Appendix B

Matlab code

This appendix contains the Matlab code developed during this thesis work. The most noteworthy scripts are included, namely the MoM solver routine (including matrix manipulation) and the fitness function.

B.1 MoM solver

```
1 function [Y,I,Imap] = MoMsolver_v2(meshdata,Z1,Z2,individual)
2 % [Y,I] = MoMsolver_v2(meshdata,Z1,Z2,individual)
3 % Solves the MoM linear system and provides the admittance
4 % matrix of the n-port
5 % where port 1 is the excitation, and the remaining are the
6 % switch ports
7 % INPUT:
8 % - meshdata: structure containing the mesh information
9 % of the structure
10 % - Z1: MoM matrix for volume 1
11 % - Z2: MoM matrix for volume 2
12 % - individual: chromosome of the individual to analyze
13 % OUTPUT:
14 % - Y: admittance matrix of the 'reduced' system after
15 % optimization
16 % - I: vector of current coefficients for each port
17 % - Imap: array for mapping the current coefficient to the
18 % basis
19 % functions
20 %% Geometry manipulation
21 % Change of optimized cells properties. Different treatment
22 % for dielectric
```

```
18 % and PEC cells
19 % PEC: 1->present 0->removed
20 % Dielectric: 1->PEC over dielectric 0->only dielectric
21 if isfield(meshdata,'sectorCell')
22     die_mask = meshdata.cellType == 1; %mask for optimizable
        dielectric cells
23     pec_mask = meshdata.cellType == 2; %mask for optimizable
        PEC cells
24
25     %PEC cells changed when 0
26     opt_mask = false(length(pec_mask),1);
27     opt_mask([meshdata.sectorCell{individual==0}]) = true; %
        optimization mask for PEC
28     pec_mask = pec_mask & opt_mask; %true for changing cells
29     %dielectric cells changed when 1
30     opt_mask = false(length(die_mask),1);
31     opt_mask([meshdata.sectorCell{individual==1}]) = true; %
        optimization mask for dielectric
32     die_mask = die_mask & opt_mask; %true for changing cells
33
34     newCellType = meshdata.cellType;
35     % change die to PEC/die 1->3
36     newCellType(die_mask) = 3;
37     % remove PEC 2->0
38     newCellType(pec_mask) = 0;
39 end
40
41 if isfield(meshdata,'sectorFunc')
42     die_mask = (meshdata.funcType == 1) | (meshdata.funcType
        == 4); %mask for optimizable dielectric functions
43     pec_mask = (meshdata.funcType == 2) | (meshdata.funcType
        == 5); %mask for optimizable PEC functions
44
45     opt_mask = false(length(pec_mask),1);
46     opt_mask([meshdata.sectorFunc{individual==0}]) = true; %
        optimization mask for PEC
47     opt_mask([meshdata.sectorBoundary{individual==0}]) = true
        ;
48     pec_mask = pec_mask & opt_mask; %true for changing cells
49
50     opt_mask = false(length(die_mask),1);
51     opt_mask([meshdata.sectorFunc{individual==1}]) = true; %
        optimization mask for dielectric
52     opt_mask([meshdata.sectorBoundary{individual==1}]) = true
        ;
53     die_mask = die_mask & opt_mask; %true for changing cells
```

```

54
55     changed_mask = die_mask | pec_mask;
56     changedFunc = unique(find(changed_mask == 1));
57 end
58
59 %% port information computation
60 Vin=1; %input voltage, just for clarity (can be omitted)
61 Nrow=max(meshdata.funcs(:,8)); %number of unknowns
62 Nport=size(meshdata.ports,1); %total number of ports
63
64 % check which ports are still present
65 portOpt = [];
66 for iPort=1:Nport
67     %check which port has been removed after optimization
68     portFunc=meshdata.ports{iPort}(:,1);
69     if ~all(ismember(portFunc,changedFunc)) %port still
70         present
71         portOpt = [portOpt iPort]; %add port to remaining
72         ports
73     elseif iPort==1
74         warning('Port 1 (feed) has been removed by
75         optimization');
76     end
77 end
78 Nport = length(portOpt); %number of ports after optimization
79
80 %% creation of port RHS vectors
81 V = zeros(Nrow,Nport); %matrix of excitation vectors
82 portID = zeros(Nport,Nrow);
83 for iPort=1:Nport
84     portFunc = meshdata.ports{portOpt(iPort)}(:,1); %port
85     function index
86     l = meshdata.ports{portOpt(iPort)}(:,4); %function side
87     length
88     u = meshdata.ports{portOpt(iPort)}(:,5); %port reference
89     direction
90
91     rowFunc = meshdata.funcs(portFunc,8);
92     V(rowFunc,iPort) = Vin*l.*u; %excitation vector of port
93
94     % compute vector that identifies each port taking into
95     account the
96     % reference direction and length
97     portID(iPort,rowFunc) = (l.*u)'; %vector for port current
98     extrapolation
99 end

```

```

92
93 %% Z matrix manipulation
94 rowMap = 1:Nrow;
95 Imap = cell(Nrow,1);
96 for iRow = 1:Nrow %loop on matrix rows
97     rowFunc = find(meshdata.funcs(:,8)==iRow); %select
          function associated with same unknown
98
99     if all(ismember(rowFunc,changedFunc)) %function is
          changed
100         % cells of function (only on one side because they
          change in the same way)
101         cells = meshdata.funcs(rowFunc(1),1:2);
102         cellsType = newCellType(cells);
103         % check new function type
104         newFuncType = evalFuncType(cellsType(1),cellsType(2))
          ;
105
106         % evaluate possible changes
107         if (meshdata.funcType(rowFunc(1))==2) && (newFuncType
          == 0) %PEC removed
108             % only electric current, don't need to check
109             Z1(rowMap(iRow),:,:) = []; %remove row and column
          from region 1
110             Z1(:,rowMap(iRow),:) = [];
111             Z2(rowMap(iRow),:,:) = []; %remove row and column
          from region 2
112             Z2(:,rowMap(iRow),:) = [];
113
114             V(rowMap(iRow),:) = []; %remove row from
          excitation vector
115             portID(:,rowMap(iRow))=[]; %remove portID column
116             % update map to new row configuration
117             rowMap(iRow+1:end) = rowMap(iRow:end-1);
118             Imap(rowMap(iRow)) = [];
119
120         elseif (meshdata.funcType(rowFunc(1))==1) && (
          newFuncType == 3) %add PEC on dielectric
121             if meshdata.funcs(rowFunc(1),10)==0 %electric
          current
122                 Z2 = [Z2; Z2(rowMap(iRow),:,:)]; %add new
          independent equation in Z2
123                 Z2 = [Z2 Z2(:,rowMap(iRow),:)];
124                 Z2(rowMap(iRow),:,:) = zeros(1,size(Z2,2),
          size(Z2,3)); %set to 0 column related to J
          on other side

```

```

125         Z2(:,rowMap(iRow),:) = zeros(size(Z2,1),1,
126             size(Z2,3));
127
128         Z1 = [Z1; zeros(1,size(Z1,2),size(Z1,3))]; %
129             add row and column to the Z1 matrix
130         Z1 = [Z1 zeros(size(Z1,1),1,size(Z1,3))];
131
132         V = [V; V(rowMap(iRow),:)]; %add row to
133             excitation vector
134         portID = [portID portID(:,rowMap(iRow))]; %
135             add portID column
136         % update map information
137         Imap{rowMap(iRow)} = rowFunc(1); %add
138             electric current to map for region 1
139         Imap{size(Z1,1)} = rowFunc(2); %add electric
140             current at bottom of map for region 2
141
142     else %magnetic current
143         Z1(rowMap(iRow),:,:) = []; %remove row and
144             column from region 1
145         Z1(:,rowMap(iRow),:) = [];
146         Z2(rowMap(iRow),:,:) = []; %remove row and
147             column from region 2
148         Z2(:,rowMap(iRow),:) = [];
149
150         V(rowMap(iRow),:) = []; %remove row from
151             excitation vector
152         portID(:,rowMap(iRow))=[]; %remove portID
153             column
154
155         % update map to new row configuration
156         rowMap(iRow+1:end) = rowMap(iRow:end-1);
157         Imap(rowMap(iRow)) = [];
158     end
159 elseif (meshdata.funcType(rowFunc(1))==4) && (
160     newFuncType == 3) %add PEC on PEC/dielectric
161     % only electric current, don't need to check
162     if meshdata.funcs(rowFunc(1),10)==0 %electric
163         current
164         Z2 = [Z2; Z2(rowMap(iRow),:,:)]; %add new
165             independent equation in Z2
166         Z2 = [Z2 Z2(:,rowMap(iRow),:)];
167         Z2(rowMap(iRow),:,:) = zeros(1,size(Z2,2),
168             size(Z2,3)); %set to 0 column related to J
169             on other side

```

```

155         Z2(:,rowMap(iRow),:) = zeros(size(Z2,1),1,
156             size(Z2,3));
157         Z1 = [Z1; zeros(1,size(Z1,2),size(Z1,3))]; %
158             add row and column to the Z1 matrix
159         Z1 = [Z1 zeros(size(Z1,1),1,size(Z1,3))];
160         V = [V; V(rowMap(iRow),:)]; %add row to
161             excitation vector
162         portID = [portID portID(:,rowMap(iRow))]; %
163             add portID column
164         % update map information
165         Imap{rowMap(iRow)} = rowFunc(1); %add
166             electric current to map for region 1
167         Imap{size(Z1,1)} = rowFunc(2); %add electric
168             current at bottom of map for region 2
169     else %magnetic current
170         error('Wrong function type definition'); %
171             magnetic current not possible on this type
172             of cell
173     end
174 elseif (meshdata.funcType(rowFunc(1))==1) && (
175     newFuncType == 4) %add PEC on dielectric for half
176     function
177     if meshdata.funcs(rowFunc(1),10)==0 %electric
178         current
179         %nothing to do, except for updating the
180         current map
181         Imap{rowMap(iRow)} = rowFunc;
182     else %magnetic current
183         Z1(rowMap(iRow),:,:) = []; %remove row and
184             column from region 1
185         Z1(:,rowMap(iRow),:) = [];
186         Z2(rowMap(iRow),:,:) = []; %remove row and
187             column from region 2
188         Z2(:,rowMap(iRow),:) = [];
189         V(rowMap(iRow),:) = []; %remove row from
190             excitation vector
191         portID(:,rowMap(iRow))=[]; %remove portID
192             column
193         % update map to new row configuration
194         rowMap(iRow+1:end) = rowMap(iRow:end-1);
195         Imap(rowMap(iRow)) = [];
196     end

```

```

185         else
186             error('Manipulation not possible');
187         end
188     else %function not changed
189         Imap{rowMap(iRow)}=rowFunc;
190     end
191 end
192 Nfreq = size(Z1,3);
193 Nfunc = size(Z1,1); %number of unknowns after optimization
194
195 %% computation of Y matrix
196 I = zeros(Nfunc,Nport,Nfreq); %initialize matrices
197 Y = zeros(Nport,Nport,Nfreq);
198 Ztot = Z1 + Z2; %PMCHWT formulation
199 Vtot = V + zeros(size(V)); %add zero forcing vector in region
    2 because there is no incident field there
200
201 for iFreq = 1:Nfreq
202     I(:, :, iFreq) = Ztot(:, :, iFreq)\Vtot; %solution of MoM
    system at each frequency
203     Y(:, :, iFreq) = (1/Vin)*portID*I(:, :, iFreq); %computation
    of Y matrix
204 end
205
206 end

```

B.2 Fitness function

```

1 function fitness = fitnessFF_4(pop,filepath,filename)
2 % Evaluates the fitness value for each individual of the
    population
3 % INPUT:
4 %   - pop: array with population chromosomes
5 %   - filepath: name of the directory of the project
6 %   - filename: name of the .mix.msh file of the structure
7 % OUTPUT:
8 %   - fitness: array with fitness values for each individual
9
10 %% global parameters
11 Z0 = 50;
12 Vin = 1; %input voltage
13

```

```

14 %% process input parameters
15 Ninds = size(pop,2); %number of individuals
16
17 simFreq = readSimFreq(filepath); %read simulation frequencies
    from file
18 Nfreq=length(simFreq);
19
20 meshdata = meshRead(filepath,filename); %read structure
    geometrical data
21
22 Z = readZmatrix(filepath); %read structure Z matrix
23 if size(Z,3)~=Nfreq
24     error('Number of Z matrices does not correspond to number
        of simulation frequencies');
25 end
26
27 wRL = 4; wDir = 0.6; %weights for return loss and directivity
28
29 phi = deg2rad(linspace(-90,90,91)); %grid points (only half
    because of symmetry)
30 theta = deg2rad(linspace(0,5,5));
31 deltaPhi = phi(2)-phi(1);
32 deltaTheta = theta(2)-theta(1);
33
34 %% loop over individuals to calculate fitness
35 fitness = ones(1,Ninds);
36 parfor iInds=1:Ninds
37     individual=pop(:,iInds); %select current individual
38
39     %% calculation of individual electrical performances
40     % solve MoM system for Y matrix
41     [Y, Jport] = MoMsolver(meshdata,Z,individual);
42     Y=squeeze(2*Y); %symmetry
43
44     Zin = 1./Y; %input impedance
45     Pin = 0.5*1*real(Y); %input power
46
47     gamma = (Zin-Z0)./(Zin+Z0); %reflection coefficient
48
49     % Far Field fitness calculation
50     Jfunc = Jport;
51     Jcell = Jfunc2cell(meshdata,Jfunc);
52
53     FFdata = FFcalculator_symm(meshdata,simFreq,Jcell,phi,
        theta);
54     fitDir = (1/Pin)*...

```

```
55         sum(FFdata.Emag(:).^2*deltaPhi*deltaTheta.*sin(FFdata
56             .Theta(:))); %far field power
57     % Fitness calculation
58     fit = (1-abs(gamma)^2)^wRL * fitDir^wDir;
59
60     % Fitness assignment
61     fitness(iInds) = -fit; %worst far field
62 end
63 end
```

Bibliography

- [1] IEEE standard for definitions of terms for antennas. *IEEE Std 145-2013 (Revision of IEEE Std 145-1993)*, pages 1–50, March 2014.
- [2] Constantine A. Balanis. *Antenna Theory: Analysis and Design, 3rd Edition*. Wiley-Interscience, 2005.
- [3] Constantine A. Balanis. *Advanced Engineering Electromagnetics*. Wiley, 2012.
- [4] M. J. Buckley. Linear array synthesis using a hybrid genetic algorithm. In *IEEE Antennas and Propagation Society International Symposium. 1996 Digest*, volume 1, pages 584–587 vol.1, July 1996.
- [5] Centre Internacional de Mètodes Numèrics a l'Enginyeria CIMNE. Gid. the personal pre and post processor. <https://www.gidhome.com/>.
- [6] Altair Engineering. Feko. <https://www.feko.info/>.
- [7] Roger F. Harrington. On gain and beamwidth of directional antennas. 6:219 – 225, 08 1958.
- [8] Walton Gibson. *The method of moments in electromagnetics*. Chapman & Hall/CRC, Boca Raton, 2008.
- [9] Roger Harrington. *Field computation by moment methods*. IEEE Press, Piscataway, NJ, 1993.
- [10] Jian-Ming Jin. *Theory and Computation of Electromagnetic Fields*. Wiley-IEEE Press, 2010.
- [11] J. M. Johnson and Y. Rahmat-Samii. Genetic algorithms and method of moments (GA/MOM) for the design of integrated antennas. *IEEE Transactions on Antennas and Propagation*, 47(10):1606–1614, Oct 1999.
- [12] D. Marcano, M. Jimenez, F. Duran, and O. Chang. Synthesis of antenna arrays using genetic algorithms. In *Proceedings of First International Caracas Conference on Devices, Circuits and Systems*, pages 328–332, Dec 1995.
- [13] D. M. Pozar. Microstrip antennas. *Proceedings of the IEEE*, 80(1):79–91, Jan 1992.
- [14] J. Leonardo Araque Quijano and G. Vecchi. Optimization of an innovative type of compact frequency-reconfigurable antenna. *IEEE Transactions on Antennas and Propagation*, 57(1):9–18, Jan 2009.
- [15] S. Rao, D. Wilton, and A. Glisson. Electromagnetic scattering by surfaces of

- arbitrary shape. *IEEE Transactions on Antennas and Propagation*, 30(3):409–418, May 1982.
- [16] M. Srinivas and L.M. Patnaik. Genetic algorithms: a survey. *Computer*, 27(6):17–26, Jun 1994.
- [17] R. Tadei, F.D. Croce, and A. Grosso. *Fondamenti di ottimizzazione*. Progetto Leonardo, 2005.
- [18] D. S. Weile and E. Michielssen. Genetic algorithm optimization applied to electromagnetics: a review. *IEEE Transactions on Antennas and Propagation*, 45(3):343–353, Mar 1997.
- [19] P. Ylä-Oijala, M. Taskinen, and S. Järvenpää. Surface integral equation formulations for solving electromagnetic scattering problems with iterative methods. *Radio Science*, 40(6), nov 2005.
- [20] Pasi Ylä-Oijala, Johannes Markkanen, Seppo Järvenpää, and Sami P. Kiminki. Surface and volume integral equation methods for time-harmonic solutions of maxwell’s equations. 149:15–44, 01 2014.
- [21] Pasi Ylä-Oijala, Matti Taskinen, and Jukka Sarvas. Surface integral equation method for general composite metallic and dielectric structures with junctions. *Progress In Electromagnetics Research*, 52:81–108, 2005.